

# Strong coupling between a dielectric nanocavity and a monolayer transition metal dichalcogenide

F. Schröder,<sup>1,2</sup> P. Wyborski,<sup>1</sup> M. Xiong,<sup>1,2</sup> G. Kountouris,<sup>1,2</sup> B. Munkhbat,<sup>1</sup>  
M. Wubs,<sup>1,2</sup> P. T. Kristensen,<sup>1,2</sup> J. Mørk,<sup>1,2</sup> and N. Stenger<sup>1,2,\*</sup>

<sup>1</sup>*Department of Electrical and Photonics Engineering,  
Technical University of Denmark, Ørsteds Plads 343, 2800 Kgs. Lyngby, Denmark*

<sup>2</sup>*NanoPhoton - Center for Nanophotonics, Technical University of Denmark,  
Ørsteds Plads 345A, 2800 Kgs. Lyngby, Denmark*

(Dated: February 11, 2025)

We demonstrate strong light-matter interaction of a dielectric nanocavity with deep sub-wavelength confinement of light and excitons in a monolayer of molybdenum ditelluride (MoTe<sub>2</sub>). Avoided crossing is demonstrated with both photoluminescence and reflection measurements, from which we extract a light-matter interaction strength of  $g \approx 5$  meV. The associated Rabi splitting is twice as large as the system's losses. These values are in good agreement with numerically-obtained values with the exciton-reaction coordinate formalism, yielding 4.6 meV. The strong light-matter interaction, combined with the low losses and the sub-wavelength light confinement, could pave the way towards single-photon nonlinearities.

Keywords: Strong coupling, dielectric nanocavity, transition metal dichalcogenides

Monolayer (ML) transition-metal dichalcogenides (TMDC), consisting of one molybdenum atom and two chalcogen atoms per unit cell, are direct bandgap semiconductors in the 2H phase [1, 2]. Their unique excitons with high binding energy [3, 4], a high absorption coefficient [5, 6], and a large oscillator strength [7, 8], make them compelling platforms for exploring strong light-matter interactions [9]. Strong coupling occurs when the energy exchange between light and excitons is fast enough to surpass the system's decay rate, resulting in Rabi oscillations and hybridized polariton states [10–12]. This regime has been demonstrated with excitons in ML TMDCs coupled to optical microcavities, where light is confined on length scales similar to the wavelength of the light [13–17]. Similarly, TMDCs integrated with plasmonic structures, such as surface plasmon-polaritons [18, 19] and plasmonic nanocavities [20–23], can exhibit strong light-matter interactions. In the latter case, light is confined on deep sub-wavelength length scales, though the confinement is accompanied by significant metal-induced losses.

Integrating dielectric cavities, such as photonic crystal cavities [24, 25] and nanobeam cavities [26] with ML MoTe<sub>2</sub> is particularly promising due to its excitonic transition energy in the near-infrared [27]. This has led, for example, to weak coupling and enhanced spontaneous emission [28]. While recent advances have explored the

light-matter interactions of ML TMDCs with dielectric nanobeam cavities [29, 30], strong coupling in these systems has not yet been achieved. Recently, confinement of light on sub-wavelength scales with dielectric materials was realized [31–37]. Topology-optimization has been demonstrated as a versatile tool for designing these extreme dielectric confinement (EDC) cavities [38–40]. These topology-optimized EDC cavities have been experimentally realized in silicon [36] and indium phosphide (InP) [37]. The sub-wavelength confinement in these novel EDC cavities, previously only achievable with plasmonic structures [41–43], comes without the associated ohmic and absorption losses intrinsic to plasmonic materials, thereby enabling unprecedented light-matter interactions [44–48]. In particular, a recent study demonstrated lasing from a quantum well embedded in such an EDC cavity [49]. Integrating EDC cavities with ML TMDCs could provide a promising platform for exploring nonlinearities [50]. The interaction of a cavity mode confined on nanometer length scales, combined with small losses, was shown to enhance exciton-exciton interactions within the ML TMDC, enabling the observation of a polariton blockade [44, 51].

In this work, we experimentally demonstrate strong coupling between an InP-based EDC cavity with sub-wavelength confinement and excitons in ML MoTe<sub>2</sub>, exploiting a design inspired by topology-optimization [54]. The avoided crossing of the system is demonstrated with temperature-resolved photoluminescence and reflection measurements, with the excitonic transition and the cavity mode being in resonance at  $T = 40$  K. The extracted

---

\* Correspondence email address: niste@dtu.dk

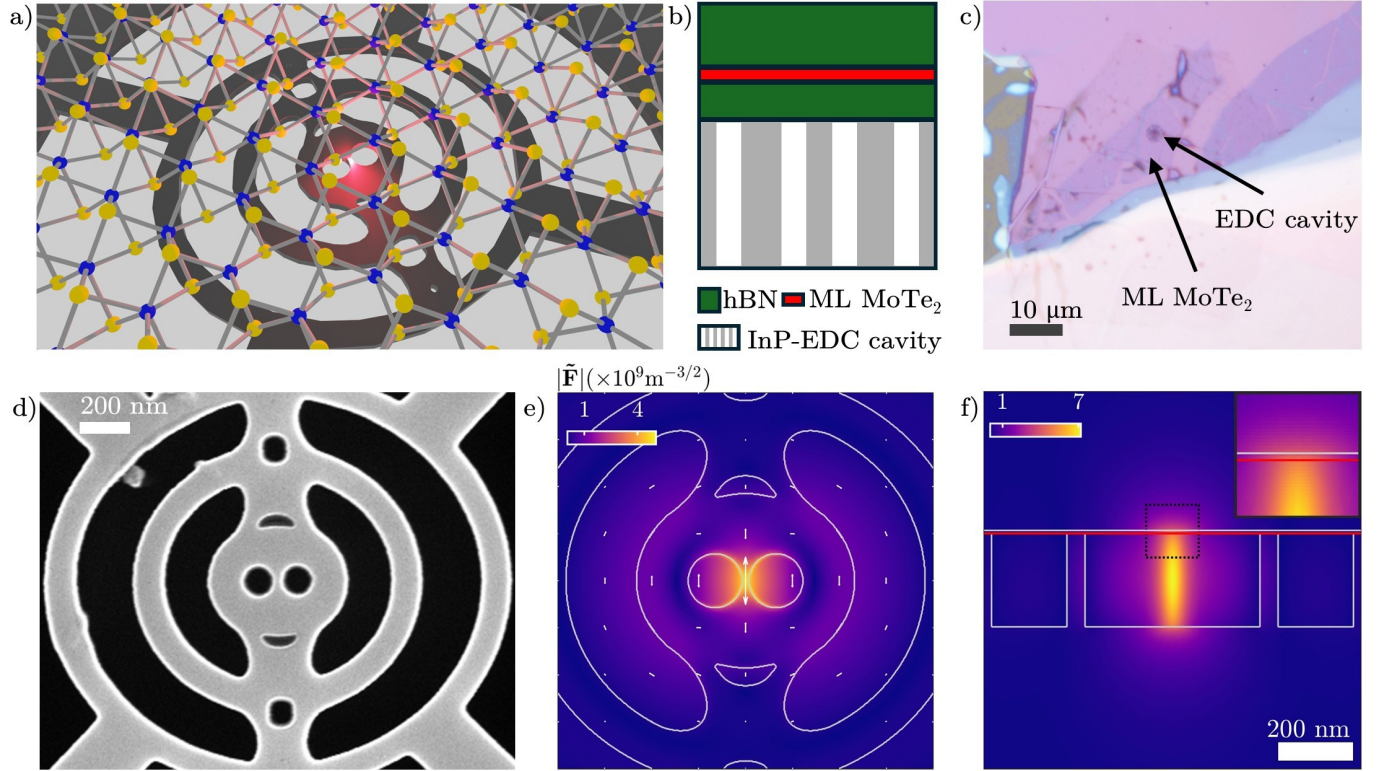


Figure 1. a) Artistic representation of the system. Light is confined in an EDC cavity. The ML MoTe<sub>2</sub> lies on top of the EDC cavity [52, 53]. The hBN flakes are not depicted. b) Sketch of the side view of the structure. c) Microscope image of the hBN-encapsulated ML MoTe<sub>2</sub> on the EDC cavity. d) SEM image of the passive cavity. Simulated electric-field distribution of the structure in e) the  $xy$ -plane at  $z = z_{2D}$  and f) the  $yz$ -plane at  $x = 0$ . Contour lines show the topography of the cavity and the hBN layer. Arrows in (e) depict the in-plane polarization of the electric-field. The red line in (f) depicts the ML MoTe<sub>2</sub>.

light-matter interaction strength is  $\approx 5$  meV, which is on the same order as obtained for a ML TMDC on a nanobeam cavity [29, 30]. The obtained Rabi-splitting is twice as large as the losses of the system. Polarization projection of the fluorescence signal enables direct comparison of the emission from the polaritons with the uncoupled exciton. The suppression of two branches and the emergence of a single peak at the center of the two polariton branches confirm the polaritonic nature of the system. The experimentally obtained value is in agreement with numerical simulations based on the reaction-coordinate formalism [50].

An artistic representation of the ML MoTe<sub>2</sub> on an EDC cavity is depicted in Fig. 1(a). ML MoTe<sub>2</sub> is sandwiched in hexagonal Boron Nitride (hBN) to prevent degradation of the monolayer [55] and to reduce the linewidth [28, 56–58]. The resulting hBN/MoTe<sub>2</sub>/hBN heterostructure is placed on the EDC cavity, cf. Fig. 1(b). The MoTe<sub>2</sub> layer is separated by  $< 2.8$  nm from the surface of the struc-

tured InP, and we refer to the  $z$  position of the ML MoTe<sub>2</sub> as  $z_{2D}$ . Please see Sec. S1 in the Supplementary Information for details on the 2D material fabrication process. A microscope image of the resulting sample is depicted in Fig. 1(c). Due to the large extent of the ML MoTe<sub>2</sub> compared to the cavity mode, the excitons are considered delocalized in the plane but strictly confined in the  $z$ -direction [50]. Nevertheless, the exciton-polaritons are laterally confined by the sub-wavelength cavity mode.

The EDC cavity is fabricated in a 245 nm thick InP membrane [37]. This material system is chosen because the excitonic transition in MoTe<sub>2</sub> is below the bandgap of InP. Therefore, the system is not limited by absorption losses of the dielectric material. We adopt the design reported in Ref. [54, 59], which is a simplified design of a topology-optimized cavity reported in Ref. [36]. Scaling it appropriately while aiming for a spacing of 20 nm between the two void regions in the cavity's center yields a design where the cavity resonance energy matches the excitonic

transition of the A-exciton in ML MoTe<sub>2</sub> at cryogenic temperatures. A scanning electron microscope (SEM) image of a similar cavity on the same chip can be found in Fig. 1(d).

The dominant response of the optical nanocavity can be accurately described by a single quasinormal mode (QNM) [60–65] with complex eigenenergy of the form  $\tilde{E}_{\text{cav}} = E_{\text{cav}} - i\Gamma_{\text{cav}}/2$ , in which  $E_{\text{cav}}$  denotes center position and  $\Gamma_{\text{cav}}$  is the full width at half maximum (FWHM) of the emission spectrum in the single-mode approximation. From numerical calculations, as detailed in the Supplementary Information, we find that the structure supports a QNM with nominal resonance energy of  $E_{\text{cav}} = 1.187$  eV, a nominal quality  $Q$  factor of  $Q = 575$ , and an effective mode volume of  $V_{\text{eff}} = 0.07(\lambda/n)^3$ . We note, however, that dielectric nanocavities often exhibit significantly lower  $Q$  factors than predicted by simulations [36, 37]. Additionally, due to the extreme field concentration, the resonance frequency is highly sensitive to small variations [54]. Fig. 1(e) and (f) show  $|\tilde{\mathbf{F}}(\mathbf{r})|$  in the  $xy$  plane at  $z_{2\text{D}}$  and in the  $yz$  plane at  $x = 0$ , respectively. The arrows in Fig. 1(e) depict  $\text{Re}[F_{x,y}(\mathbf{r})]$ , highlighting the linear polarization of the cavity  $\tilde{E}_{\text{cav}}$  along the  $y$  axis [54, 59]. In addition, the structure supports another mode in the spectral vicinity with orthogonal polarization at a lower resonance energy and with a lower quality factor, which we have rigorously studied in Ref. [59] and labeled as the low- $Q$  mode.

For excitons in ML TMDCs and dielectric nanocavities, the light-matter interaction strength  $g$  can be calculated using the QNMs, together with material-specific properties of the ML TMDC [50, 66]. In this study, we follow Ref. [50] and describe the light-matter interaction in a reaction-coordinate formalism, in which  $g_{\text{theory}}$  can be expressed as

$$g_{\text{theory}} = \sqrt{\frac{\hbar^2 e_0^2}{\pi \epsilon_0 m_0^2 E_{\text{cav}} a_{\text{B}}^2} \sum_{\alpha} \int d^2\mathbf{r} \left| \tilde{\mathbf{F}}(\mathbf{r}_{xy}, z_{2\text{D}}) \cdot \mathbf{p}_{\text{cv}}^{\alpha} \right|^2}, \quad (1)$$

where  $\mathbf{p}_{\text{cv}}^{\alpha}$  denotes the transition dipole moment of the ML TMDC,  $\alpha$  denotes the valley index  $K, K'$  [67], and  $a_{\text{B}}$  denotes the excitonic Bohr radius of the A-exciton. The integral is performed in the  $xy$  plane of the ML MoTe<sub>2</sub> (cf. Fig. 1(e)), indicated as the red line in Fig. 1(f). From Eq. 1 it follows that the light-matter interaction strength strongly depends on the polarization of the cavity mode. If we consider, for example a linearly-polarized cavity mode with  $\tilde{\mathbf{F}}(\mathbf{r}_{xy}, z_0) = F_0(\mathbf{r}_{xy}, z_0)\hat{e}_y$ , then  $g$  reaches its maximal value of  $\mathbf{p}_{\text{cv}}^{\alpha} \parallel \hat{e}_y$  and vanishes for  $\mathbf{p}_{\text{cv}}^{\alpha} \perp \hat{e}_y$ . Eq. 1 is solved numerically, yielding  $g_{\text{theory}} = 4.61(6)$  meV, see Sec. S2 in the Supplementary

Information for details on the numerical calculations.

We investigate PL spectra as a function of temperature  $T$  with the detection polarization  $\hat{E}_{\text{det}}$  oriented with  $\hat{E}_{\text{cav}}$ . Temperature variations primarily affect the excitonic emission energy  $E_{\text{exc}}$  through the bandgap temperature dependence and modify the exciton linewidth  $\Gamma_{\text{exc}}$  due to phonon interactions. In contrast, the cavity resonance energy  $E_{\text{cav}}$  is influenced by the temperature dependence of the refractive index, but its variation is much smaller compared to the changes in  $E_{\text{exc}}$ . We explore these dependencies systematically, which allows us to calculate the detuning  $\delta = E_{\text{cav}} - E_{\text{exc}}$ , see Sec. S3 in the Supplementary Information for details. Fig. 2(a) depicts spectra as a function of detuning in a range of  $T = 4 - 163$  K. In addition, Fig. 2(b) shows PL spectra in a region of interest close to zero detuning, as indicated in panel (a). In both panel (a) and (b), fits from reference measurements of the uncoupled cavity and of the uncoupled excitons are shown as black dashed and solid lines, respectively. We go from negative detuning to positive values in the measured temperature range, with  $T = 40$  K corresponding to  $\delta = -0.2(7)$  meV. Clearly, avoided crossing is observed, which is a hallmark of strong light-matter coupling.

We use two different setups for different temperature regimes as indicated in Fig. 2(a), see Appendix for details. Setup 1 contains a liquid-helium cryostat for  $T \leq 70$  K, corresponding to  $\delta \leq 5.2(8)$  meV. Setup 2 contains a liquid-nitrogen cryostat for  $T \geq 79$  K, corresponding to  $\delta \geq 6.2(10)$  meV. Slight deviations in the photon energy measured with different setups may arise from imperfect spectrometer alignment. We quantify this offset to be approximately 3 meV; see Sec. S3 in the Supplementary Information for details. The data from Setup 2 in Fig. 2(a) and (c) have been corrected accordingly.

To assess the light-matter interaction strength, we fit the extracted peak positions of the lower ( $E_-$ ) and of the upper ( $E_+$ ) polariton with the real part of a coupled-oscillator model, see Sec. S4 and S5 in the Supplementary Information for details. The fit result, indicated as the red lines in Fig. 2(a) and (b), yields  $g_{\text{PL}} = 5.3(3)$  meV.

The PL measurements are supplemented with reflection measurements in a cross-polarization configuration, see Appendix for details [59]. Fig. 2(b) and (c) depict reflection spectra as a function of  $\delta$ . As observed from PL measurements, the avoided crossing is clearly visible as two dips in the reflection spectra, confirming hybridization of excitons and photons. A fit of the reflection measurements with the coupled-oscillator model yields  $g_{\text{R}} = 4.7(7)$  meV, which agrees well with the value obtained from PL measurements. Notably, the experimentally obtained values  $g_{\text{R}}$  and  $g_{\text{PL}}$  are in good agreement

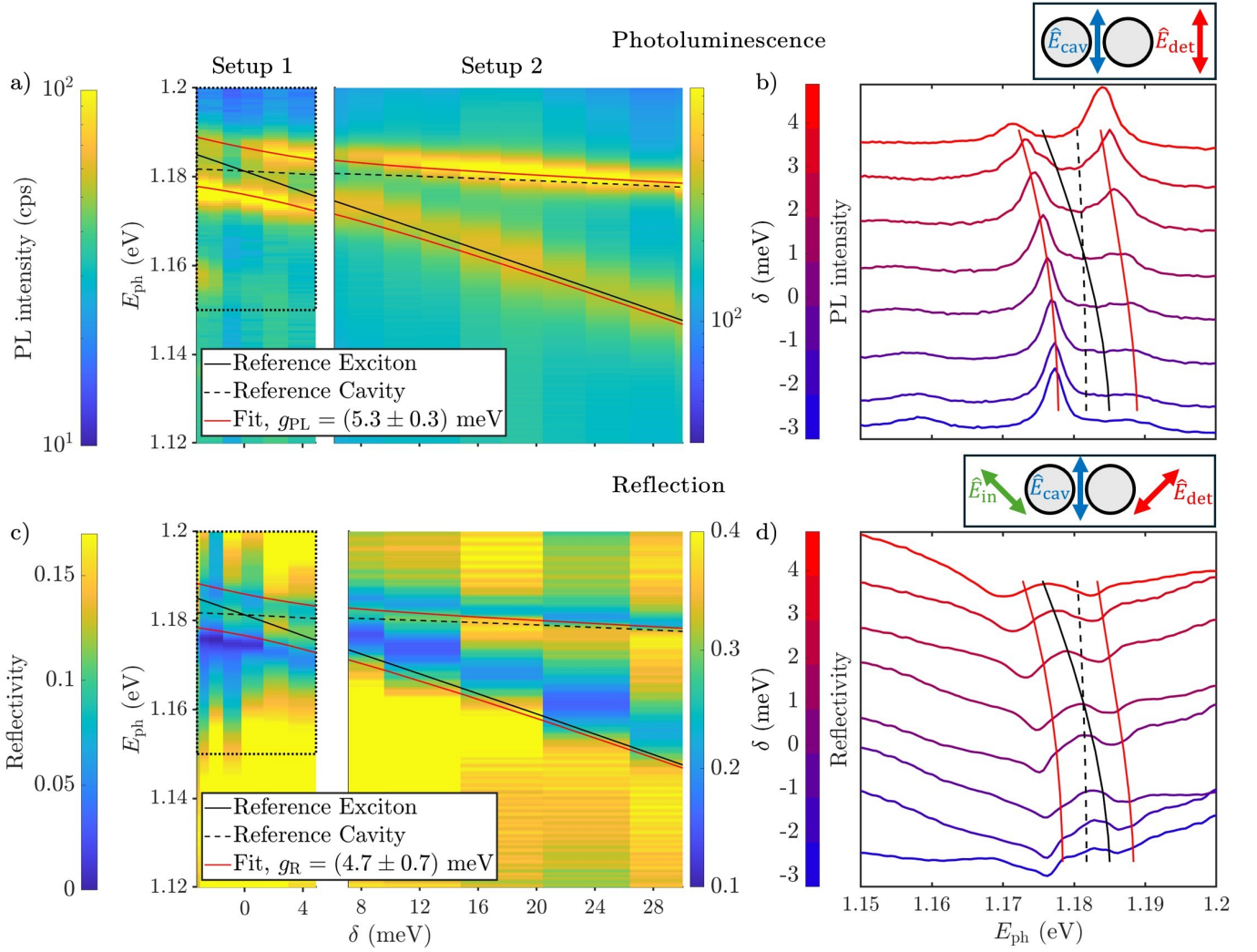


Figure 2. a) and b) PL spectra as a function of detuning, recorded with the detection polarization aligned with the cavity mode. The dotted box in (a) depicts the region of the spectra depicted in (b). The solid and dashed black line depicts the reference for the exciton and for the cavity mode, respectively, see Sec. S3 in the Supplementary Information. c) and d) Reflectivity spectra recorded in a cross-polarization configuration. Setup 1 and 2 are explained in the main text.

with the value obtained with the exciton-reaction coordinate formalism  $g_{theory}$  (see above).

Strong coupling is usually referred to when the number of oscillations in the polariton states  $N_{Rabi}$  is larger than one [68]. This is achieved when [10, 11, 22]

$$N_{Rabi} = \frac{2E_{Rabi}}{\Gamma_{exc} + \Gamma_{cav}} \geq 1 \Leftrightarrow E_{Rabi} \geq \frac{\Gamma_{exc} + \Gamma_{cav}}{2}, \quad (2)$$

with  $E_{Rabi} = \sqrt{4g^2 - (\Gamma_{cav} - \Gamma_{exc})^2}/4$  denoting the Rabi splitting. To assess the Rabi splitting, the cavity and exciton linewidth are evaluated at  $T = 40$  K/  $\delta =$

$-0.2(7)$  meV, yielding  $\Gamma_{cav} = 3.3(1)$  meV and  $\Gamma_{exc} = 6.0(7)$  meV see Sec. S4 in the Supplementary information for details. Together with the determined values for  $g$ , we find  $E_{Rabi} = 10.6(7)$  meV and  $9.4(15)$  meV as deduced from PL and reflection measurements, respectively. This value agrees well with the energy splitting of the polaritonic emission determined from the peak positions at  $\delta = -0.2(7)$  meV,  $E_+ - E_- = 10.1(3)$  meV and  $9.4(7)$  meV for PL and reflection measurements, respectively.  $E_{Rabi}$  overcomes the averaged losses in the system by more than a factor of two as  $E_{Rabi} > (\Gamma_{exc} + \Gamma_{cav})/2 = 4.7(4)$  meV.

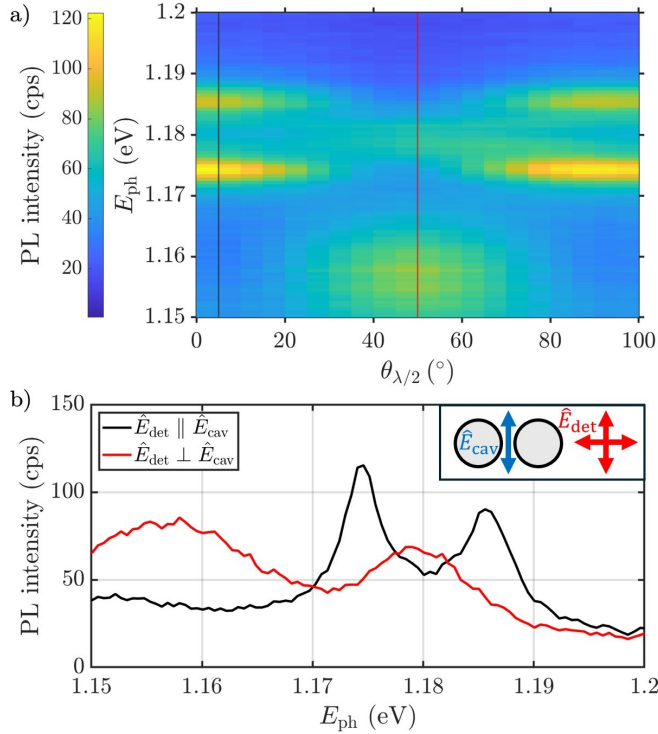


Figure 3. a) PL spectra at  $T = 50$  K as a function of  $\theta_{\lambda/2}$  in front of the analyzer. b) PL spectra from (a) with the analyzer oriented parallel and perpendicular to the cavity mode for black and red lines, respectively.

We deduce  $N_{\text{Rabi}} = 2.3(1)$  and  $2.0(2)$  for PL and reflection measurements, respectively, yielding around two oscillations of the coupled system. Conclusively, the system is in the strong-coupling regime.

We note that in general, the light-matter interaction strength is complex-valued [46, 66, 69]. To evaluate the magnitude of the complex part of the light-matter interaction strength, we fit the extracted peak positions and the linewidths, corresponding to the real and the imaginary parts of the eigenvalues, respectively, see Sec. S5 in the Supplementary Information for details. We find that the coupled-oscillator model also fits the linewidths accurately, which is additional confirmation of the reported strong light-matter interaction. Moreover, we find that the imaginary part of the light-matter interaction strength is less than 6% of the real part and is almost zero within the error bars, which justifies neglecting the imaginary part of the light-matter interaction strength.

We turn our attention to the polarization properties of the photoluminescence signal. As the cavity mode is linearly polarized, orienting the detection polarization per-

allel to the cavity mode polarization enables the study of the strongly coupled system. On the other hand, by orienting the detection polarization perpendicular to the cavity mode, primarily residual excitons, that do not couple to the cavity mode are detected. Those are excited in the ML MoTe<sub>2</sub> in the vicinity of the cavity mode. The emission is studied at  $T = 50$  K, corresponding to  $\delta = 1.4(7)$  meV. Fig. 3 depicts spectra as a function of the angle of the halfwave ( $\lambda/2$ ) plate  $\theta_{\lambda/2}$  in front of the analyzer. Together with the analyzer, rotating the  $\lambda/2$  plate by  $\theta_{\lambda/2}$  effectively rotates the detection polarization state by twice that value. Two peaks, separated by 11 meV and associated with the polaritonic emission, are identified for  $\hat{E}_{\text{cav}} \parallel \hat{E}_{\text{det}}$ , corresponding to  $2\theta_{\lambda/2} = 10^\circ$  and  $190^\circ$ , see Fig. 3. Rotating the detection polarization by  $2\theta_{\lambda/2} = 90^\circ$ , yields a detection polarization perpendicular to the orientation of the cavity mode. One peak centered between the two polaritonic peaks is detected, corresponding to emission from residual excitons that do not couple to the cavity mode. Another peak is observed at  $E_{\text{ph}} = 1.157$  eV for  $\hat{E}_{\text{det}} \perp \hat{E}_{\text{cav}}$ . This is well explained by another mode in the cavity. In Ref. [59], we demonstrate that the EDC cavity supports a low- $Q$  mode close to the mode investigated in this work (high- $Q$  mode), which has lower eigenenergy, lower  $Q$ -factor, and orthogonal polarization. The low- $Q$  mode could be excited by trions, which are known to exist at lower transition energy than excitons in the ML MoTe<sub>2</sub> [70].

In summary, we demonstrate that excitons in a ML MoTe<sub>2</sub> interact strongly with light confined by an EDC cavity on sub-wavelength length scales. The light-matter interaction strength is deduced both from photoluminescence and reflection measurements, yielding  $g_{\text{PL}} = 5.3(3)$  meV /  $g_{\text{R}} = 4.7(7)$  meV. With a numerical calculation exploiting the exciton-reaction coordinate formalism [50], we show that these values can be accurately calculated, yielding  $g_{\text{theory}} = 4.6$  meV. Polarization-projection of the fluorescence signal confirms the polaritonic nature of the coupled system. The strongly interacting system, combined with sub-wavelength light confinement and minimal losses, is expected to exhibit intense exciton-exciton interactions, potentially enabling the observation of single-photon nonlinearities [44].

## ACKNOWLEDGEMENTS

We thank Dorte R. Danielsen, Duc Hieu Nguyen, and Manh-Ha Dohan for the fruitful discussion about 2D material fabrication, as well as Peter Bøggild and Timothy J. Booth for their support. This work was supported by the [Danish National Research Foundation](#)

through NanoPhoton - Center for Nanophotonics, grant number D NRF147. N. S. acknowledges funding by the Novo Nordisk Foundation NERD Programme (project QuDec NNF23OC0082957). P.W. and B.M. acknowledge support from the European Research Council (ERC-StG *TuneTMD*, grant no. 101076437), and the Vilum Foundation (grant no. VIL53033). P.W. and B.M. also acknowledge the European Research Council (ERC-CoG *Unity*, grant no. 865230) and Carlsberg Foundation (grant no. CF21-0496).

## APPENDIX: EXPERIMENTAL SETUPS

Two setups are used to access the temperature regime from room temperature to 4 K. Setup 1 contains a closed-cycle liquid-helium cryostat (AttoDRY800XS, *Attocube*), giving us access to  $T \leq 70$  K. Setup 2 contains a liquid-nitrogen cryostat (HFS600, *Linkam Scientific*), allowing us to measure  $T \geq 79$  K. In both setups, the system is excited with a red laser ( $\lambda_{\text{laser}} = 650$  and 637.5 nm for Setups 1 and 2, respectively). The excitation light beam is directed via a dichroic mirror (Setup 1)/ a 50/50 beam-splitter (Setup 2) to a microscope objective, focusing the light on the sample. The emitted light is, after polarization projection with a  $\lambda/2$  plate and a linear polarizer

(= analyzer), detected by a spectrometer. A longpass filter ensures the filtering of the excitation light beam. We note that small deviations of the recorded wavelengths are likely to occur when comparing spectra recorded in both setups due to imperfect alignment of the spectrometers, see Sec. S3 in the Supplementary Information for quantification of this offset.

Adaptions to our PL setups allow us to carry out reflection measurements. For that, we change the light source to a superluminescent diode (SLD1050P, *Thorlabs*). In addition to the analyzer and the  $\lambda/2$  plate in the detection path, we insert a linear polarizer and a  $\lambda/2$  plate in the excitation path, as well as a quarter-wave ( $\lambda/4$ ) plate in the detection path. In Setup 1, the dichroic mirror is exchanged with a 50/50 beamsplitter. The reflection measurements are carried out in a cross-polarization configuration, where the polarization of the incoming light  $\hat{E}_{\text{in}}$  is perpendicular to the detection polarization  $\hat{E}_{\text{det}}$ , for example  $\hat{E}_{\text{in}} = \hat{x}$ ,  $\hat{E}_{\text{det}} = \hat{y}$ . The sample is oriented so that the linear polarization of the cavity mode is oriented  $45^\circ$  with respect to both of them, e.g.  $\hat{E}_{\text{cav}} = \frac{1}{\sqrt{2}}(\hat{x} + \hat{y})$  [59, 71]. The quarter-wave plate is carefully adjusted to suppress elliptically polarized elements induced by scattering at the glass window of the cryostat. All spectra have been normalized with a reference spectrum recorded on a gold surface.

---

## Supplementary Information: Strong coupling between a dielectric nanocavity and a monolayer transition metal dichalcogenide

### S1. 2D MATERIAL FABRICATION

In this Supplementary Information, the 2D material fabrication process is described. Firstly, MoTe<sub>2</sub> and hBN (*HQ Graphene*) are mechanically exfoliated on polydimethylsiloxane (PDMS) on a glass slide and on a 300 nm silicon dioxide (SiO<sub>2</sub>) on a silicon (Si) wafer, respectively (cf. Fig. S1(a)-(c)). The thicknesses of the hBN flakes are determined with the optical contrast method [72]. Using a calibrated microscope [73], we deduce thicknesses of 1.5(13) nm and 9.0(5) nm for the lower and the upper hBN flake, respectively. The 2D materials are stacked using a commercially available transfer system (*HQ Graphene*). The monolayer MoTe<sub>2</sub> is placed on the thin hBN flake with a dry-transfer method [74]. The lower hBN flake on the substrate is placed on a hot plate on a three-axis micrometer stage. Another three-axis micrometer stage holds the glass slide with the MoTe<sub>2</sub> flake. The lower hBN flake and the ML MoTe<sub>2</sub> are aligned with an optical microscope and pressed together. Then, the hotplate is heated up to 60 °C to ensure that the ML sticks to the hBN flake, see Fig. S1(d). After that, the upper hBN flake is picked up with a polycarbonate (PC)/polydimethylsiloxane (PDMS) film [75, 76]. The stamp is pressed on the upper hBN flake at 60 °C. The hotplate is set to 110 °C when contact is established. After 5 minutes, the substrate is moved down, and the hBN flake sticks to the PC film. The hBN/MoTe<sub>2</sub> heterostructure (HS) is picked up by the upper hBN flake on a PC/PDMS film, pressing them together at 110 °C. After waiting for 5 minutes and moving the substrate down again, the hBN-encapsulated ML MoTe<sub>2</sub> is formed on the PC film, see Fig. S1(e). The hBN/MoTe<sub>2</sub>/hBN HS is then pressed on the EDC cavity at 110 °C. The temperature is then set to 190 °C so that the PC film melts. After 20-30 seconds, the sample is moved away, and the HS remains on the cavity. After that, the sample is cleaned in chloroform for more than 20 minutes

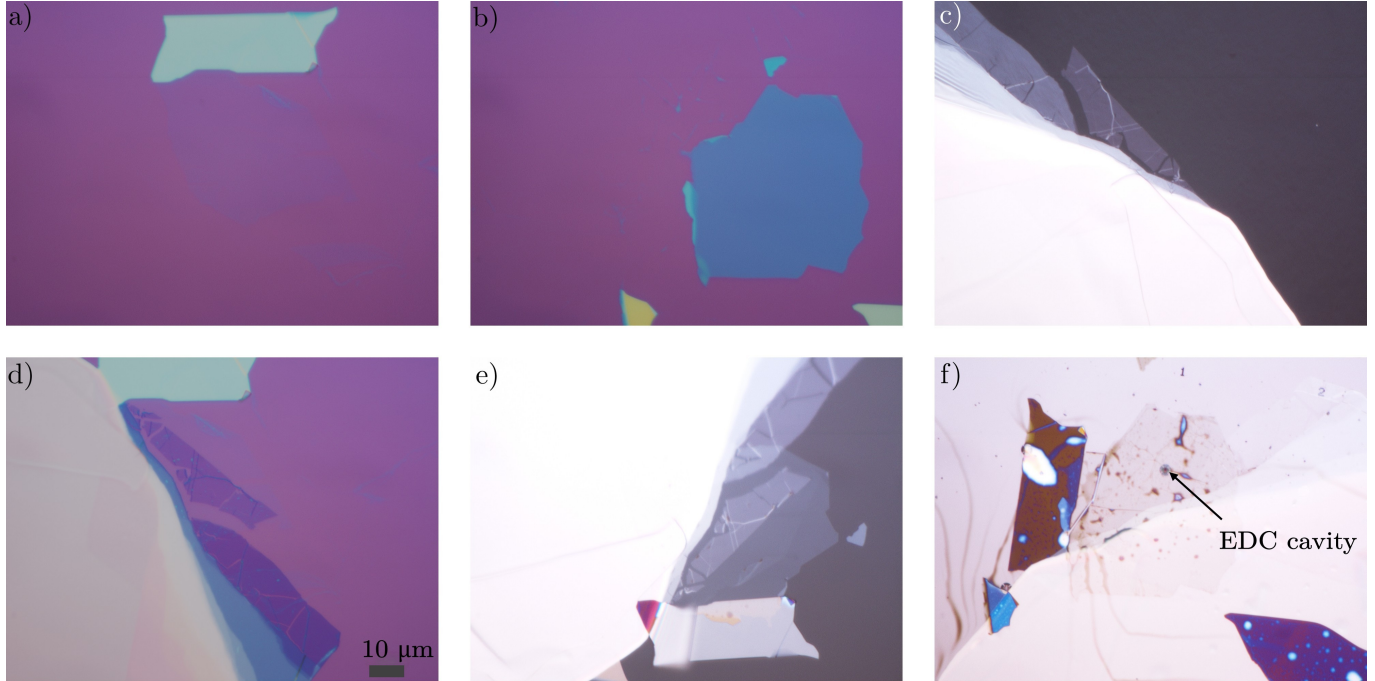


Figure S1. Microscope image with 100x magnification after each fabrication step. a) Lower hBN flake on a 300 nm SiO<sub>2</sub>/Si substrate. The flake of interest is the faint purple region in the center of the image. b) Upper hBN flake on a 300 nm SiO<sub>2</sub>/Si substrate. c) MoTe<sub>2</sub> on a PDMS substrate. d) MoTe<sub>2</sub> on lower hBN on a 300 nm SiO<sub>2</sub>/Si substrate. e) hBN/MoTe<sub>2</sub>/hBN heterostructure on the PC/PDMS stamp. f) Heterostructure on the EDC cavity.

and washed with isopropanol (IPA), see Fig. S1(e). The image in Fig. 1(c) in the main text depicts the final result, where Fig. S1(d) and (f) are overlaid with each other for better visibility of the ML MoTe<sub>2</sub>.

PL spectra at room temperature of the bare EDC cavity before stacking the HS on top, and of the excitonic emission from a monolayer MoTe<sub>2</sub> are compared with the combined system as fabricated, cf. Fig. S2. Clearly, the excitonic emission and the cavity mode can be observed together, demonstrating the successful deposition of the HS on the EDC cavity. It is evident that even without the excitonic emission from MoTe<sub>2</sub>, PL signal from the EDC cavity can be observed. We attribute this to spontaneous recombination in the dielectric material due to the above-bandgap excitation of InP. A Lorentzian fit of the cavity mode emission of the fabricated sample (cf. Fig. S2(c)) reveals a resonance energy of  $E_{\text{cav}} = 1.166 \text{ eV}$  and a full-width half-maximum  $\Gamma_{\text{cav}} = 3.4 \text{ meV}$ , yielding a quality factor of  $Q = 348(7)$ . It is evident from Fig. S2 that depositing the 2D HS on the EDC cavity blueshifts the resonance energy by  $\approx 10 \text{ meV}$ , resulting from the increase of the effective refractive index of the cavity mode [54]. Moreover, encapsulating the MoTe<sub>2</sub> flake with hBN and depositing the HS on the EDC cavity blueshifts the excitonic transition by  $\approx 6 \text{ meV}$ , see Fig. S2, which can be explained by screening of the Coulomb interaction of the electron-hole pairs in the ML TMDC [4, 5, 77].

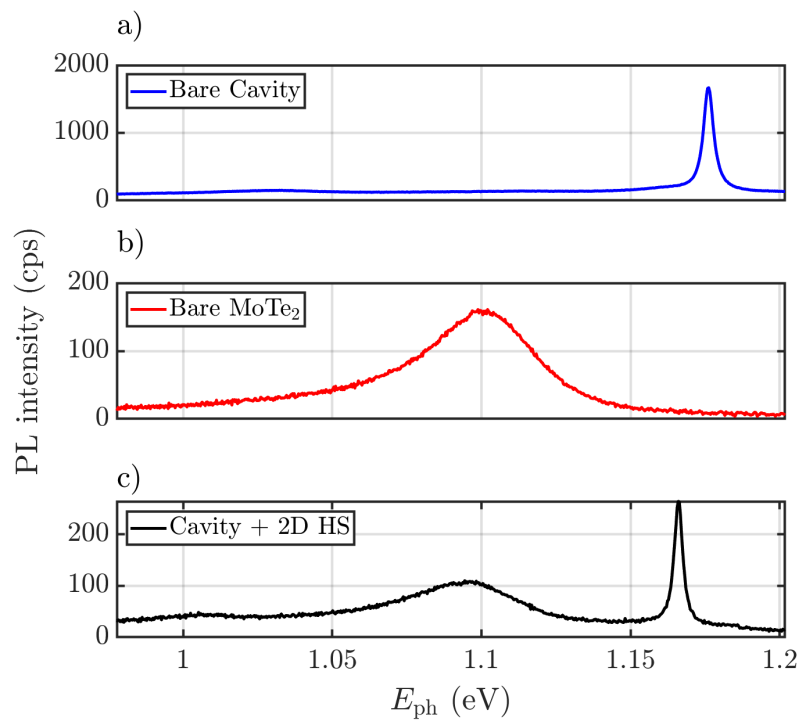


Figure S2. PL spectra at room temperature, of a) the EDC cavity before stacking the hBN/MoTe<sub>2</sub>/hBN heterostructure on top, of b) a MoTe<sub>2</sub> layer on PDMS and of c) the combined system.

## S2. DETAILS ON SIMULATIONS

The electric-field QNMs  $\mathbf{f}_j(\mathbf{r})$  are the solutions to the source-less wave equation

$$\nabla \times \nabla \times \tilde{\mathbf{f}}_j(\mathbf{r}) - \tilde{k}_j^2 \epsilon_{\mathbf{R}}(\mathbf{r}) \tilde{\mathbf{f}}_j(\mathbf{r}) = 0 \quad (\text{S1})$$

subject to suitable radiation conditions [64], in which  $\epsilon_{\mathbf{R}}(\mathbf{r})$  is the spatially-dependent relative permittivity and the index  $j$  labels the different QNMs with corresponding wavenumber  $\tilde{k}_j^2 = \tilde{\omega}_j/c$ , where  $\tilde{\omega}_j$  is the complex eigenfrequency. Even for purely real permittivities, the complex frequencies account for a finite dissipation due to radiation, which means that the field leaks away from the cavity and eventually diverges at large distances. Nevertheless, the QNMs can be normalized by one of several complementary formulas [78]. This also has implications for the expression for the coupling strength in Eq. (1), for which the divergent integral was regularized by use of a quasistatic approximation to the Green tensor in Ref. [50]. For the present calculation, the field is so localized, that we ignore this issue and calculate the coupling strength simply by an integral across the extend of the cavity using the normalized field profile  $\tilde{\mathbf{F}}_j(\mathbf{r}) = \tilde{\mathbf{f}}_j(\mathbf{r})/\sqrt{\langle\langle \tilde{\mathbf{f}}_j | \tilde{\mathbf{f}}_j \rangle\rangle}$ , in which  $\sqrt{\langle\langle \tilde{\mathbf{f}}_j | \tilde{\mathbf{f}}_j \rangle\rangle}$  denotes the normalization.

For the eigenmode analysis, we used a finite-element method calculation with the commercial software COMSOL Multiphysics, solving Eq. S1 numerically following the approach in Ref. [54]. The thicknesses of hBN layers are determined as described in Sec. S1. For simplification, the thin ML MoTe<sub>2</sub> (thickness of 0.65 nm [27]) does not enter the eigenmode calculation.

The simulation domain includes the structured 245 nm thick InP membrane and an hBN layer with a thickness of 10.5 nm. Moreover, scattering boundary conditions are applied, see [54] for details on the simulation approach. The integral in Eq. 1 in the main text is evaluated at  $z_{2D} = 1.5$  nm above the cavity surface, corresponding to the thickness of the lower hBN flake. The constants  $a_B$  and  $\mathbf{p}_{\text{cv}}^\alpha$  are calculated with values from [27, 79–81]. The refractive index of hBN and InP can be found in Ref. [82] and [83, 84], respectively.

A convergence study is carried out as described in Ref. [54], yielding  $E_{\text{cav}}^{\text{sim}} = (1.186867 \pm 6 \times 10^{-6})$  eV,  $\Gamma_{\text{cav}}^{\text{sim}} = 2.06(4)$  meV,  $V_{\text{eff}} = (0.07 \pm 0.01)(\lambda/n)^3$  and  $g_{\text{theory}} = 4.61(6)$  meV. We note that the uncertainty presented is the numerical error. As described in the main text, deviations are likely to occur, for example, due to fabrication imperfections and surface roughnesses. These uncertainties are expected to be larger than the numerical uncertainty for a given geometry.

### S3. REFERENCE MEASUREMENTS

In this Supplementary Information, the reference measurements for deducing  $E_{\text{exc}}(T)$ ,  $E_{\text{cav}}(T)$ ,  $\Gamma_{\text{exc}}(T)$  and  $\Gamma_{\text{cav}}(T)$  are described.

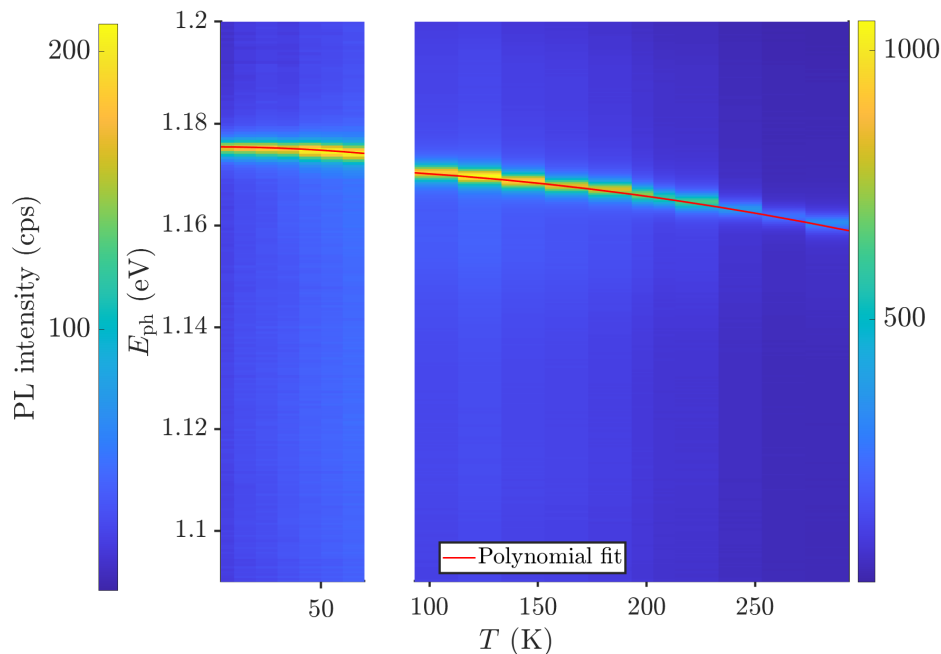


Figure S3. PL spectra as a function of temperature from the reference cavity. The red line indicates a fit of the peak position with a parabola.

Fig. S3 depicts spectra as a function of temperatures of a reference cavity. For those measurements, the detection polarization is aligned with the polarization of the cavity mode. Each spectrum is fitted with a single Lorentzian (cf. Fig. S10), yielding  $E_{\text{cav,ref}}(T)$  and  $\Gamma_{\text{cav,ref}}(T)$  (see Fig. S4), where the subscript "ref" indicates that these values are obtained from a reference cavity.  $E_{\text{cav,ref}}(T)$  is fitted with a parabola,  $E_{\text{cav,ref}}(T) = y_0 + bT^2$ . The obtained temperature dependence of the resonance energy is indicated by the red line in Fig. S3 and Fig. S4(a). Moreover, as evident from Fig. S4(b), the linewidth of the cavity does not depend on temperature as it is not limited by phonon interactions.

As two different setups are used for different temperature regimes, a shift in photon energy is observed between  $T \leq 70$  K and  $T \geq 79$  K, arising from the imperfect alignment of the respective spectrometers used in Setup 1 and 2. We quantify this offset with the temperature dependence of the reference cavity.  $E_{\text{cav,ref}}(T)$  from Setup 1 and 2 is extrapolated to 75 K, and the offset is calculated as  $E_{\text{cav,ref}}^{\text{Setup1}}(75 \text{ K}) - E_{\text{cav,ref}}^{\text{Setup2}}(75 \text{ K})$ . This yields an offset of 3 meV (cf. inset in Fig. S4), and the data from Setup 2 in Fig. 2 in the main text have been shifted accordingly.

The resonance energy of the reference cavity  $E_{\text{cav,ref}}(T)$  deviates from the resonance energy of the cavity with the hBN/MoTe<sub>2</sub>/hBN heterostructure  $E_{\text{cav}}(T)$  (cf. Fig. S5). This is partially due to the presence of the heterostructure, which changes the effective refractive index of the cavity mode, and partially due to fabrication differences of the cavities, see main text. This overall shift  $\Delta = E_{\text{cav,ref}} - E_{\text{cav}}$  is quantified at  $T = 293$  K and  $T = 315$  K for Setup 1 and Setup 2, respectively, corresponding to a detuning  $\delta > 70$  meV. From the coupled-oscillator model it follows that for large detuning, the polaritonic eigenenergies equal the eigenenergies of the respective oscillators. In other words, at this temperature, the influence of the excitonic transition on the cavity mode is negligible. This yields  $\Delta = 6.89(3)$  meV and  $\Delta = 6.3(1)$  meV for Setup 1 and Setup 2, respectively, see the gray arrow in Fig. S5. The temperature dependence of the cavity can be deduced from the temperature dependence of the reference cavity  $E_{\text{cav}}(T) = E_{\text{cav,ref}}(T) + \Delta$ .

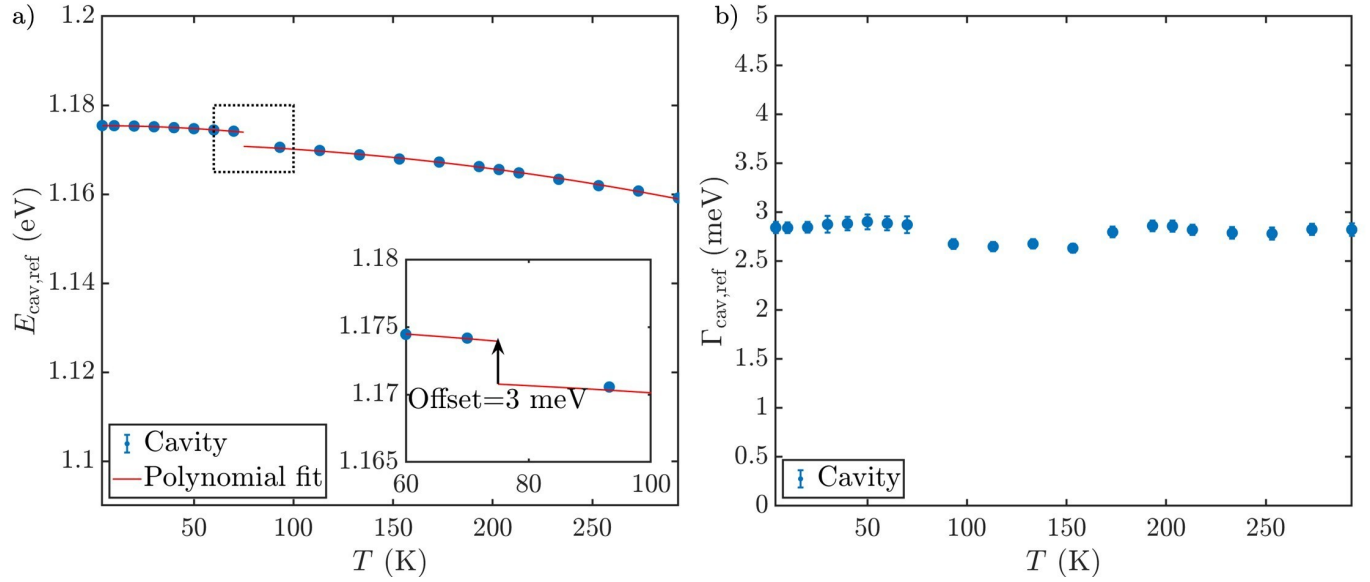


Figure S4. a) Extracted peak positions and b) linewidths of the reference cavity as a function of  $T$ . The red line in (a) depicts the fits with a parabola.

Moreover, since the linewidth of the reference cavity does not depend on the temperature, we use the value for  $\Gamma_{\text{cav}}$  deduced from the cavity with the hBN/MoTe<sub>2</sub>/hBN heterostructure at  $T = 293$  K (cf. Fig. S5) as the cavity's reference linewidth for all temperatures.

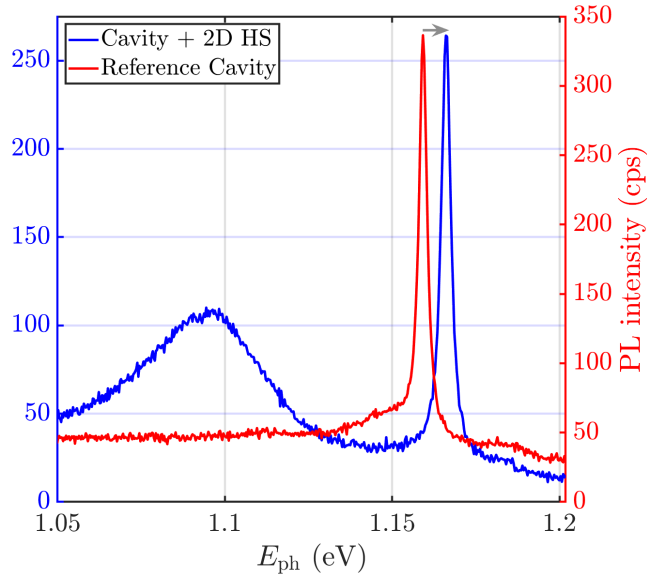


Figure S5. PL spectra at  $T = 293$  K for the reference cavity and the sample consisting of EDC cavity and the HS for red and blue lines, respectively. The offset  $\Delta$  is indicated as the grey arrow.

Fig. S6 depicts PL emission spectra of the hBN/MoTe<sub>2</sub>/hBN heterostructure on the EDC cavity with the detection

polarization perpendicular to the cavity mode. Again, a shift in photon energy is observed between  $T \leq 70$  K and  $T \geq 79$  K as described above. As described in the main text, this way we obtain emission from uncoupled excitons in the vicinity of the cavity mode. Each spectrum is fitted with two Lorentzian peaks (see also Fig. S9 for a fit at  $T = 40$  K). One peak fits the excitonic transition, and the other fits the trion transition stimulating the low- $Q$  mode. This way, the excitonic transition energy  $E_{\text{exc}}(T)$  and the linewidth  $\Gamma_{\text{exc}}(T)$  are obtained for each temperature, cf. Fig. S7. We observe that signatures of the cavity mode remain faintly visible for higher temperatures, possibly due to non-perfect polarization projection due to scattering from objects in the optical beam path, mainly from the glass window of the cryostat. The low- $Q$  mode [59] is visible throughout the whole measurement series and gets dominant at lower temperatures probably because of excitation by trions [70].

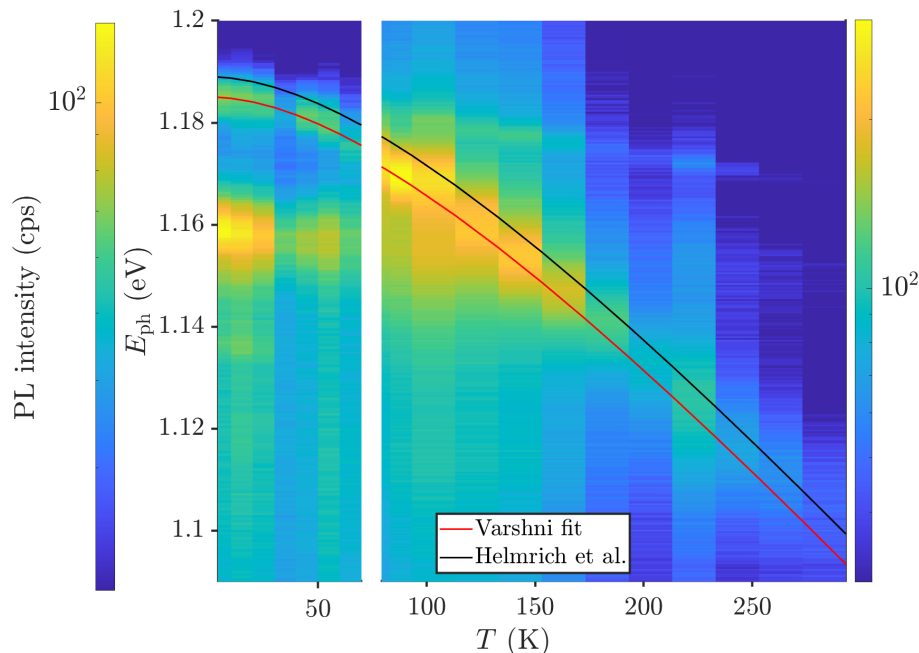


Figure S6. PL spectra as a function of temperature from the hBN/MoTe<sub>2</sub>/hBN heterostructure on the EDC cavity with the detection polarization perpendicular to the cavity mode. The red line indicates a Varshni fit of the peak position of the excitonic transition. The black line depicts the temperature dependence of the exciton in MoTe<sub>2</sub> on silicon dioxide found in Ref. [70].

As the temperature dependence of the excitonic transition energy is given by the temperature dependence of the band gap, the extracted  $E_{\text{exc}}(T)$  are fitted with the Varshni equation [70]

$$E_{\text{exc}}(T) = E_{\text{exc}}(0) - \frac{\alpha T^2}{T + \beta} \quad (\text{S2})$$

where  $E_{\text{exc}}(0)$ ,  $\alpha$  and  $\beta$  are material parameters. The temperature dependence of the exciton is expected to follow previously reported values, so  $\alpha$  and  $\beta$  are fixed [70]. This leaves  $E_{\text{exc}}(0)$  as the only free fitting parameter. The fit result is indicated as the red line in Fig. S6 and Fig. S7(a), showing good agreement with the obtained PL spectra and deviates by the values found in Ref. [70] by a constant offset. A small but constant offset is likely to occur for different samples and can be explained by a different dielectric environment, yielding differences due to screening of the Coulomb interaction [4]. The data presented in Ref. [70] are measured from a monolayer MoTe<sub>2</sub> on a SiO<sub>2</sub> substrate, whereas our flake is encapsulated in hBN and on a structured InP region (the EDC cavity). This shows that for a quantitative assessment of the reference excitonic energy and, in turn, for the extraction of the light-matter interaction strength, it is highly beneficial to extract the reference from the same sample.

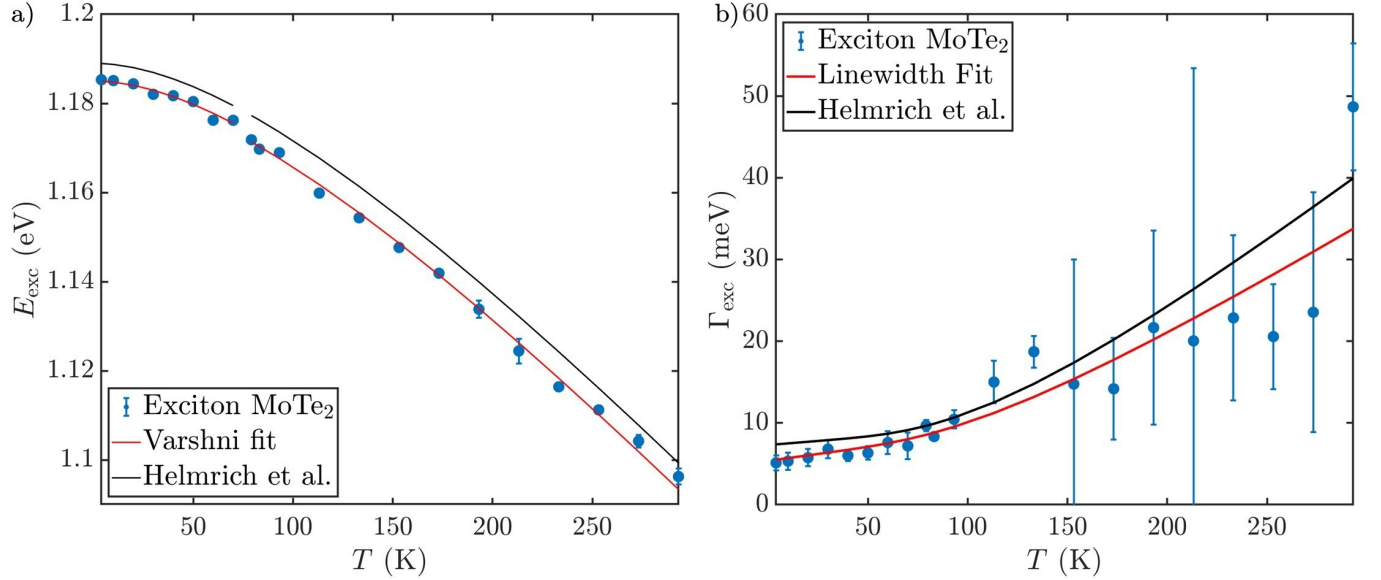


Figure S7. a) Extracted peak positions and b) linewidths of the uncoupled excitons as a function of  $T$ . The red lines depict fit results as described in the main text. The black line depicts the temperature dependence of the exciton in MoTe<sub>2</sub> on silicon dioxide found in Ref. [70].

The temperature dependence of the exciton linewidth  $\Gamma_{\text{exc}}$  is given as [70]

$$\Gamma_{\text{exc}}(T) = \Gamma_0 + \gamma_{\text{LA}} T + \frac{\Gamma_{\text{LO}}}{\exp(E_{\text{LO}}/k_B T) - 1}, \quad (\text{S3})$$

where  $\Gamma_0$  denotes the intrinsic linewidth,  $\gamma_{\text{LA}}$  the exciton-acoustic phonon strength, and the last term accounts for interaction with longitudinal optical phonons. The extracted linewidth from the spectra in Fig. S6 is depicted in Fig. S7(b). A fit with Eq. S3 is indicated as the red line, and compared to the values obtained in Ref. [70], indicated as the black line. The fit results agree qualitatively, and small deviations are likely to occur due to slightly altered exciton-phonon interaction in different samples. The fit result for  $\Gamma_{\text{exc}}$  has a large uncertainty at  $T > 150$  K due to the spectral overlap of exciton and trion emission, but gives accurate result close to the region of interest 4 – 140 K where we observe the avoided crossing (see main text).

The obtained temperature-dependencies for  $E_{\text{exc}}(T)$ ,  $E_{\text{cav}}(T)$ ,  $\Gamma_{\text{exc}}(T)$  and  $\Gamma_{\text{cav}}(T)$  allow fitting with a coupled-oscillator model with the light-matter interaction strength as the only free fitting parameter. The calculated detuning  $\delta(T) = E_{\text{cav}}(T) - E_{\text{exc}}(T)$  is summarized in Tab. I. The uncertainty for  $T$  is assumed to be  $\sigma_T = \pm 0.5$  K. The uncertainty in the detuning  $\sigma_\delta$  is calculated from the uncertainty of  $E_{\text{exc}}$ ,  $E_{\text{cav}}$  and  $T$  with Gaussian error propagation.

$T \pm 0.5$ (K)	$\delta$ (meV)	$\sigma_\delta$ (meV)
4	-3.3	0.7
10	-3.1	0.7
20	-2.4	0.7
30	-1.5	0.7
40	-0.2	0.7
50	1.3	0.7
60	3.0	0.7
70	4.9	0.7
79	6.2	1.0
83	7.1	1.0
93	9.6	1.0
103	12.1	1.1
113	14.8	1.1
123	17.6	1.1
133	20.4	1.1
143	23.4	1.1
153	26.4	1.1
163	29.5	1.1
173	32.6	1.1
193	39.0	1.1
213	45.5	1.1
233	52.1	1.1
253	58.8	1.1
273	65.6	1.1
293	72.4	1.1

Table I. Measured values for  $T$  and corresponding detuning  $\delta$  and uncertainty  $\sigma_\delta$ .

#### S4. FITS AT $T = 40$ K

In this section, we present fits of the spectra of the coupled system and of the references, exemplary at  $T = 40$  K, corresponding to  $\delta = -0.2(8)$  meV.

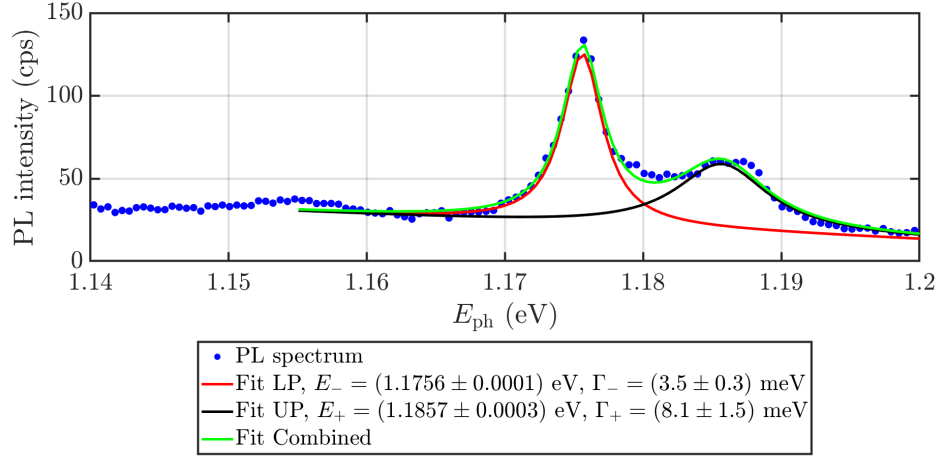


Figure S8. PL spectrum of the hBN/MoTe<sub>2</sub>/hBN heterostructure on the EDC cavity at  $T = 40$  K with the detection polarization oriented parallel to the cavity mode. Fitting the polaritonic emission is carried out as described in the main text.

Fig. S8 depicts the PL spectrum from the sample consisting of the EDC cavity and the HS with the detection polarization aligned with the polarization of the cavity mode. The lower and upper polariton peaks on a linearly-sloped background are fitted with two Lorentzian lineshapes simultaneously, indicated by the red and black lines in Fig. S8, respectively. The overall fit is indicated as the green line. From the fit, the resonance energies  $E_- = 1.176$  eV and  $E_+ = 1.186$  eV, as well as the linewidths  $\Gamma_- = 3.5(3)$  meV and  $\Gamma_+ = 8.1(15)$  meV are obtained.

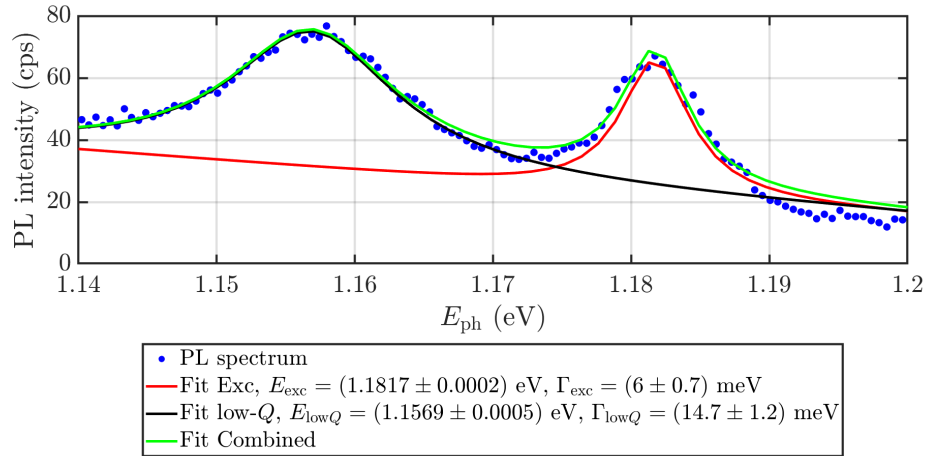


Figure S9. PL spectrum of the hBN/MoTe<sub>2</sub>/hBN heterostructure on the EDC cavity at  $T = 40$  K with the detection polarization oriented perpendicularly to the cavity mode. Fitting the excitonic emission and the low- $Q$  mode is carried out as described in the main text.

Fig. S9 depicts the PL spectrum from the sample consisting of the EDC cavity and the HS with the detection

polarization perpendicular to the polarization of the cavity mode. The excitonic emission and the low- $Q$  mode are fitted with two Lorentzian peaks on a linearly-sloped background simultaneously, indicated by the red and black lines in Fig. S9, respectively. The fit yields  $E_{\text{exc}} = 1.182 \text{ eV}$  and  $\Gamma_{\text{exc}} = 6.0(7) \text{ meV}$ .

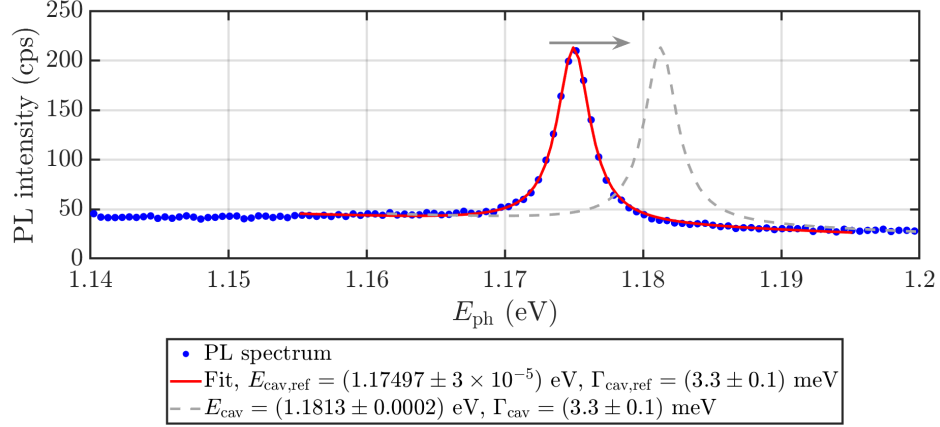


Figure S10. PL spectrum of the reference EDC cavity with the detection polarization parallel to the polarization of the cavity mode. Fitting the cavity mode is carried out as described in the main text. Moreover, the deduced lineshape for  $E_{\text{cav}}$  and  $\Gamma_{\text{cav}}$  (see Sec. S3), is indicated as the dashed grey line. The length of the grey arrow equals the shift in photon energy  $\Delta$ , cf. Fig. S5.

Fig. S10 depicts the PL spectrum from the reference EDC cavity with the detection polarization parallel to the polarization of the cavity mode. The emission from the cavity is fitted with a Lorentzian peak on a linearly sloped background, indicated by the red line in Fig. S10. The fit yields  $E_{\text{cav,ref}} = 1.175 \text{ eV}$ , from which  $E_{\text{cav,ref}}$  is deduced as  $1.181 \text{ eV}$  is deduced, see Sec. S3.

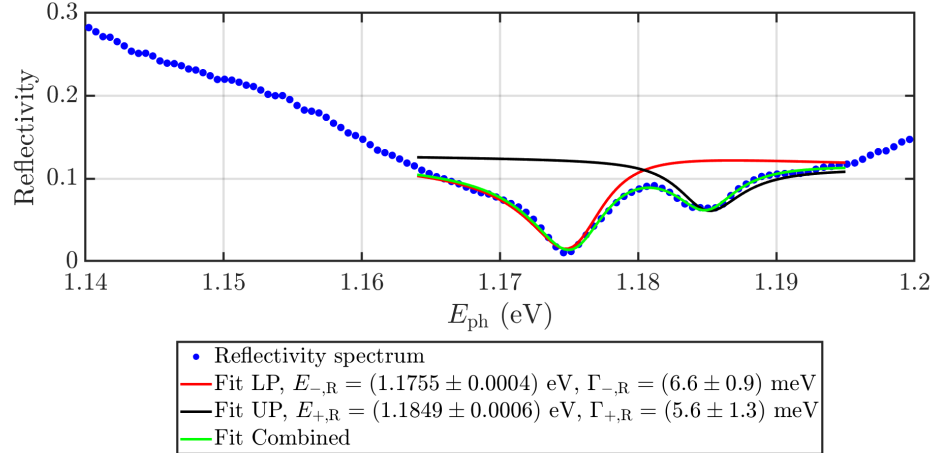


Figure S11. Reflectivity spectrum of the hBN/MoTe2/hBN heterostructure on the EDC cavity at  $T = 40 \text{ K}$  in a cross-polarization configuration. Fitting the polaritonic features is carried out as described in the main text.

Fig. S11 depicts the reflectivity spectrum from the sample consisting of the EDC cavity and the HS in a cross-polarization configuration. In reflection measurements, resonances often exhibit Fano lineshapes, resulting from a superposition of a Lorentzian resonance with a slowly-varying background [59]. Therefore, we fit the reflectivity  $R$  in

a spectral range close to  $E_-$  and  $E_+$  with the equation [85]

$$R(E_{\text{ph}}) = \left| \frac{a_- \Gamma_- / 2 e^{i\varphi_1}}{i(E_{\text{ph}} - E_-) + \Gamma_- / 2} + \frac{a_+ \Gamma_+ / 2 e^{i\varphi_2}}{i(E_{\text{ph}} - E_+) + \Gamma_+ / 2} + \frac{a_{\text{BG}} \Gamma_{\text{BG}} / 2}{i(E_{\text{ph}} - E_{\text{BG}}) + \Gamma_{\text{BG}} / 2} \right|^2. \quad (\text{S4})$$

Here,  $a_-$ ,  $a_+$  and  $a_{\text{BG}}$  denote amplitudes for the lower and the upper polaritons and the broad background, respectively, for the chosen polarization settings, and  $\varphi_1$  and  $\varphi_2$  take into account potential phase differences between the resonances. From the fit, the resonance energies  $E_{-,R} = 1.176$  eV and  $E_{+,R} = 1.185$  eV, as well as the linewidths  $\Gamma_{-,R} = 6.6(9)$  meV and  $\Gamma_{+,R} = 5.6(13)$  meV are found. The subscript "R" indicates that the values are deduced from reflection measurements. These values are in good agreement with the values determined from the PL measurements.

### S5. FIT WITH COUPLED-OSCILLATOR MODEL

The interaction of light and matter can be described by a coupled-oscillator model, where the electromagnetic field in the cavity and the excitonic transition are modeled by two individual harmonic oscillators. The eigenenergies of the coupled states are determined by the eigenvalues of the matrix [9, 66]

$$E_{\pm} = EV \left( \begin{bmatrix} E_{\text{cav}} - \frac{i\Gamma_{\text{cav}}}{2} & g \\ g & E_{\text{exc}} - \frac{i\Gamma_{\text{exc}}}{2} \end{bmatrix} \right) \quad (\text{S5})$$

Diagonalizing Eq. S5 yields the dispersion relation for the upper (+) and lower (-) polariton

$$E_{\pm} = \frac{1}{2}(E_{\text{cav}} + E_{\text{exc}}) - \frac{i}{4}(\Gamma_{\text{cav}} - \Gamma_{\text{exc}}) \pm \frac{1}{2} \sqrt{4g^2 + \left( \delta - \frac{i}{2}(\Gamma_{\text{cav}} - \Gamma_{\text{exc}}) \right)^2}. \quad (\text{S6})$$

From the dispersion relation in Eq. S6, the Rabi splitting is given by the energy difference at zero detuning

$$E_{\text{Rabi}} = E_+ - E_-|_{\delta=0} = \sqrt{4g^2 - \frac{(\Gamma_{\text{cav}} - \Gamma_{\text{exc}})^2}{4}}. \quad (\text{S7})$$

The system is referred to as strongly coupled if  $E_{\text{Rabi}} > (\Gamma_{\text{cav}} + \Gamma_{\text{exc}})/2$ , see for example Ref. [11, 86] and references therein.

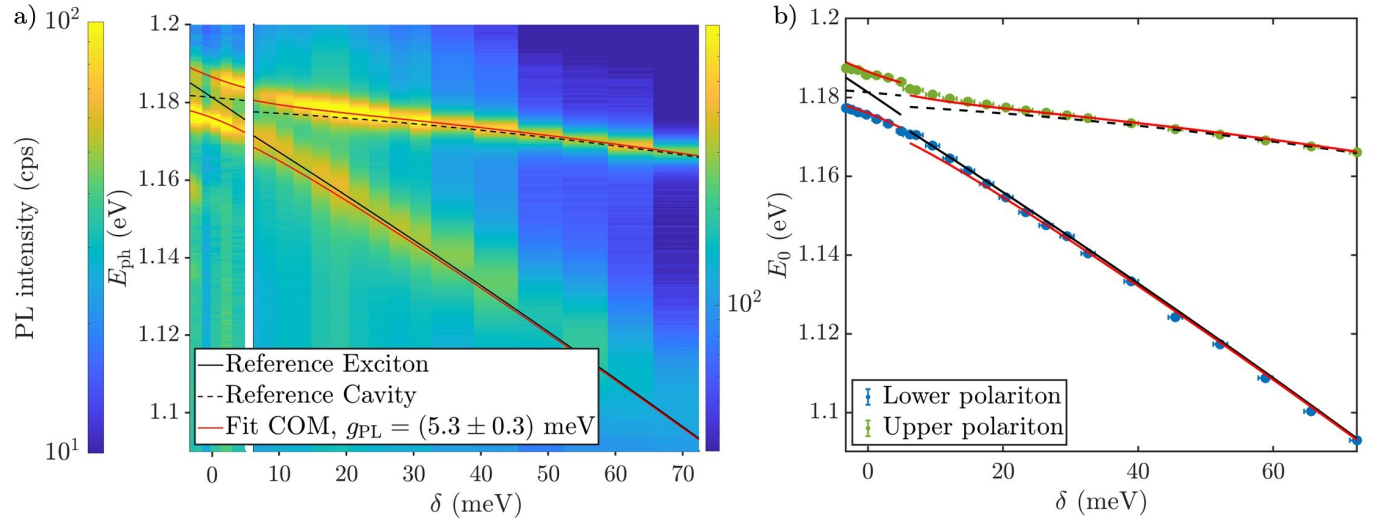


Figure S12. a) PL spectra of the coupled system as a function of detuning over the full temperature range, recorded with the detection polarization aligned with the cavity mode. b) Extracted peak positions from the PL measurements. The solid and dashed black lines depict the reference for the exciton and for the cavity mode, respectively, see Sec. S3. A fit with the real part of the coupled-oscillator model is indicated by the red lines.

Fig. S12(a) depicts PL spectra shown in Fig. 2 in the main text over the full temperature range, together with fits from reference measurements of the uncoupled cavity and of the uncoupled excitons. As described in Sec. S3, a shift in photon energy of  $\approx 3$  meV is observed between  $T \leq 70$  K and  $T \geq 79$  K, due to imperfect alignment of the respective spectrometers used in Setup 1 and 2. The extracted peak positions from a Lorentzian fit (cf. Fig. S8) are

depicted in Fig. S12(b). Together with the obtained values for  $E_{\text{cav}}$ ,  $E_{\text{exc}}$ ,  $\Gamma_{\text{cav}}$  and  $\Gamma_{\text{exc}}$  (see Sec. S3), these are fitted with the real part of the dispersion relation (Eq. S6), leaving  $g$  as the only free fitting parameter. The fit of the PL measurements, indicated by the red lines, yields  $g_{\text{PL}} = 5.3(3)$  meV.

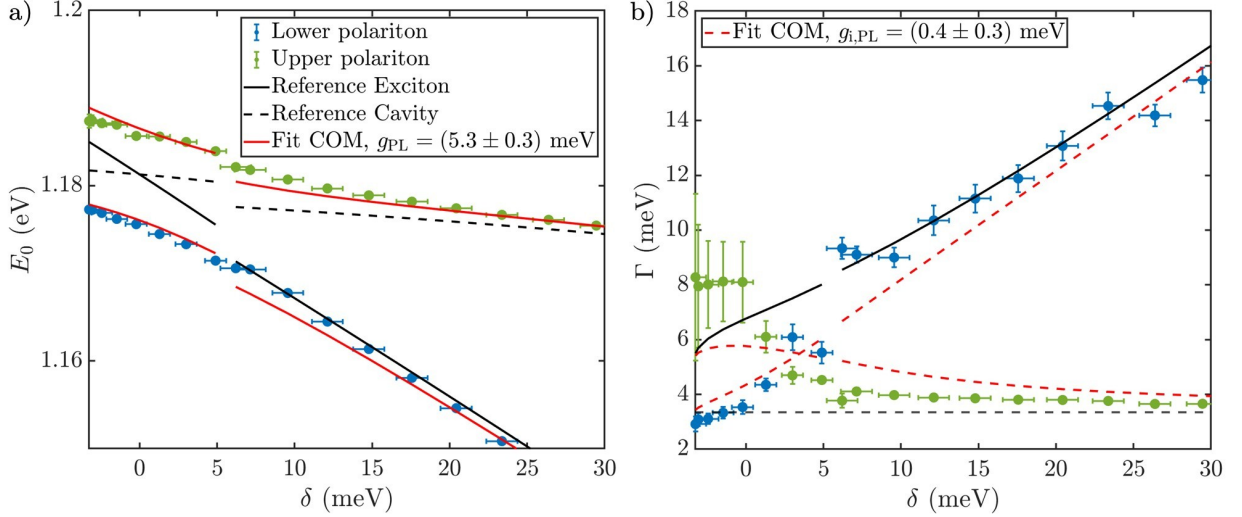


Figure S13. a) Extracted peak positions and b) FWHM of the PL measurements of the coupled system in a region of interest around zero detuning. A fit with the full complex coupled-oscillator model is indicated as solid and dashed red lines for the real and the imaginary parts, respectively.

In general, the light-matter interaction strength is complex  $\tilde{g} = g - ig_i$  [46, 69]. To evaluate the magnitude  $g_i$ , the complex eigenvalues  $\tilde{E}_- = E_- - i\Gamma_-/2$  and  $\tilde{E}_+ = E_+ - i\Gamma_+/2$  are fitted with the real and imaginary parts of the dispersion relation (Eq. S6) simultaneously with a complex fit parameter  $\tilde{g}$ , exemplary for the PL measurements. Fig. S12(a) depicts the extracted peak positions corresponding to  $\text{Re}(\tilde{E}_\pm)$  and (b) shows the extracted linewidth, corresponding to  $-2 \text{Im}(\tilde{E}_\pm)$ . The fit, indicated as the red solid and dashed lines in (a) and (b), respectively, yields  $\tilde{g} = ((5.3 - 0.3i) \pm (0.4 + 0.3i))\text{meV}$ . The coupled-oscillator model describes the imaginary part of the spectrum very well, which is additional confirmation of the reported strong light-matter interaction. As the imaginary part of  $\tilde{g}$  is less than 6% of the real part and is almost zero within the error bars, it is justified to focus on the real part of the coupled-oscillator model in this case.

Fig. S14(a) depicts reflectivity spectra shown in Fig. 2 in the main text over the full temperature range. The extracted peak positions from a Fano fit (cf. Fig. S11) are depicted in Fig. S14(b). A fit with the real part of the coupled-oscillator model is carried out similarly as for the PL measurements, yielding  $g_{\text{R}} = 4.7(7)$  meV. For the reflection measurements, the fit is restricted to  $T < 180$  K since the signal-to-noise ratio of the lower polariton becomes small, which is associated with large uncertainties in the fit parameters.

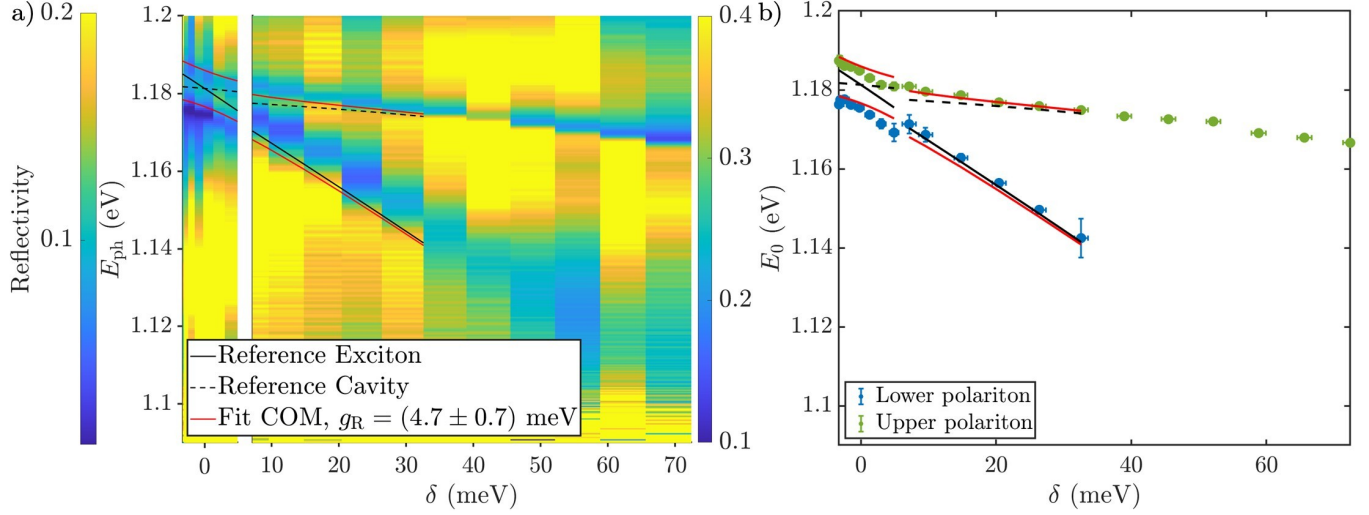


Figure S14. a) Reflectivity spectra of the coupled system as a function of detuning over the full temperature range, recorded with the detection polarization aligned with the cavity mode. b) Extracted peak positions from the reflectivity measurements. The solid and dashed black lines depict the reference for the exciton and for the cavity mode, respectively, see Sec. S3. A fit with the real part of the coupled-oscillator model is indicated by the red lines.

- 
- [1] A. Splendiani, L. Sun, Y. Zhang, T. Li, J. Kim, C. Y. Chim, G. Galli, and F. Wang, Emerging photoluminescence in monolayer MoS<sub>2</sub>, *Nano Lett.* **10**, 1271 (2010).
  - [2] K. F. Mak, C. Lee, J. Hone, J. Shan, and T. F. Heinz, Atomically Thin MoS<sub>2</sub>: A New Direct-Gap Semiconductor, *Phys. Rev. Lett.* **105**, 136805 (2010).
  - [3] K. He, N. Kumar, L. Zhao, Z. Wang, K. F. Mak, H. Zhao, and J. Shan, Tightly Bound Excitons in Monolayer WSe<sub>2</sub>, *Phys. Rev. Lett.* **113**, 026803 (2014).
  - [4] A. Chernikov, T. C. Berkelbach, H. M. Hill, A. Rigosi, Y. Li, B. Aslan, D. R. Reichman, M. S. Hybertsen, and T. F. Heinz, Exciton Binding Energy and Nonhydrogenic Rydberg Series in Monolayer WSe<sub>2</sub>, *Phys. Rev. Lett.* **113**, 076802 (2014).
  - [5] Y. Li, A. Chernikov, X. Zhang, A. Rigosi, H. M. Hill, A. M. van der Zande, D. A. Chenet, E.-M. Shih, J. Hone, and T. F. Heinz, Measurement of the optical dielectric function of monolayer transition-metal dichalcogenides: MoS<sub>2</sub>, MoSe<sub>2</sub>, WS<sub>2</sub> and WSe<sub>2</sub>, *Phys. Rev. B* **90**, 205422 (2014).
  - [6] B. Munkhbat, P. Wróbel, T. J. Antosiewicz, and T. O. Shegai, Optical Constants of Several Multilayer Transition Metal Dichalcogenides Measured by Spectroscopic Ellipsometry in the 300–1700 nm Range: High Index, Anisotropy, and Hyperbolicity, *ACS Photonics* **9**, 2398 (2022).
  - [7] C. Robert, D. Lagarde, F. Cadiz, G. Wang, B. Lassagne, T. Amand, A. Balocchi, P. Renucci, S. Tongay, B. Urbaszek, and X. Marie, Exciton radiative lifetime in transition metal dichalcogenide monolayers, *Phys. Rev. B* **93**, 1 (2016).
  - [8] C. Robert, R. Picard, D. Lagarde, G. Wang, J. P. Echeverry, F. Cadiz, P. Renucci, A. Högele, T. Amand, X. Marie, I. C. Gerber, and B. Urbaszek, Excitonic properties of semiconducting monolayer and bilayer MoTe<sub>2</sub>, *Phys. Rev. B* **94**, 1 (2016).
  - [9] C. Schneider, M. M. Glazov, T. Korn, S. Höfling, and B. Urbaszek, Two-dimensional semiconductors in the regime of strong light-matter coupling, *Nat. Commun.* **9**, 2695 (2018).
  - [10] P. Törmä and W. L. Barnes, Strong coupling between surface plasmon polaritons and emitters: a review, *Reports Prog. Phys.* **78**, 013901 (2015).
  - [11] P. A. Gonçalves, N. Stenger, J. D. Cox, N. A. Mortensen, and S. Xiao, Strong Light–Matter Interactions Enabled by Polaritons in Atomically Thin Materials, *Adv. Opt. Mater.* **8**, 1 (2020).
  - [12] C. Tserkezis, A. I. Fernández-Domínguez, P. A. Gonçalves, F. Todisco, J. D. Cox, K. Busch, N. Stenger, S. I. Bozhevolnyi, N. A. Mortensen, and C. Wolff, On the applicability of quantum-optical concepts in strong-coupling nanophotonics, *Reports Prog. Phys.* **83**, (2020).
  - [13] X. Liu, T. Galfsky, Z. Sun, F. Xia, E.-c. Lin, Y.-H. Lee, S. Kéna-Cohen, and V. M. Menon, Strong light–matter coupling

- in two-dimensional atomic crystals, *Nat. Photonics* **9**, 30 (2015).
- [14] S. Dufferwiel, S. Schwarz, F. Withers, A. A. P. Trichet, F. Li, M. Sich, O. Del Pozo-Zamudio, C. Clark, A. Nalitov, D. D. Solnyshkov, G. Malpuech, K. S. Novoselov, J. M. Smith, M. S. Skolnick, D. N. Krizhanovskii, and A. I. Tartakovskii, Exciton–polaritons in van der Waals heterostructures embedded in tunable microcavities, *Nat. Commun.* **6**, 8579 (2015).
- [15] M. Sidler, P. Back, O. Cotlet, A. Srivastava, T. Fink, M. Kroner, E. Demler, and A. Imamoglu, Fermi polaron-polaritons in charge-tunable atomically thin semiconductors, *Nat. Phys.* **13**, 255 (2017).
- [16] L. Zhang, R. Gogna, W. Burg, E. Tutuc, and H. Deng, Photonic-crystal exciton-polaritons in monolayer semiconductors, *Nat. Commun.* **9**, 713 (2018).
- [17] H. Shan, I. Iorsh, B. Han, C. Rupperecht, H. Knopf, F. Eilenberger, M. Esmann, K. Yumigeta, K. Watanabe, T. Taniguchi, S. Klembt, S. Höfling, S. Tongay, C. Antón-Solanas, I. A. Shelykh, and C. Schneider, Brightening of a dark monolayer semiconductor via strong light-matter coupling in a cavity, *Nat. Commun.* **13**, 3001 (2022).
- [18] R. B. Iyer, Y. Luan, R. Shinar, J. Shinar, and Z. Fei, Nano-optical imaging of exciton–plasmon polaritons in WSe<sub>2</sub>/Au heterostructures, *Nanoscale* **14**, 15663 (2022).
- [19] L. N. Casses, B. Zhou, Q. Lin, A. Tan, D.-P. Bendixen-Fernex de Mongex, K. J. Kaltenecker, S. Xiao, M. Wubs, and N. Stenger, Full Quantitative Near-Field Characterization of Strongly Coupled Exciton–Plasmon Polaritons in Thin-Layered WSe<sub>2</sub> on a Monocrystalline Gold Platelet, *ACS Photonics* **11**, 3593 (2024).
- [20] J. Wen, H. Wang, W. Wang, Z. Deng, C. Zhuang, Y. Zhang, F. Liu, J. She, J. Chen, H. Chen, S. Deng, and N. Xu, Room-Temperature Strong Light–Matter Interaction with Active Control in Single Plasmonic Nanorod Coupled with Two-Dimensional Atomic Crystals, *Nano Lett.* **17**, 4689 (2017).
- [21] M. Stührenberg, B. Munkhbat, D. G. Baranov, J. Cuadra, A. B. Yankovich, T. J. Antosiewicz, E. Olsson, and T. Shegai, Strong Light-Matter Coupling between Plasmons in Individual Gold Bi-pyramids and Excitons in Mono- and Multilayer WSe<sub>2</sub>, *Nano Lett.* **18**, 5938 (2018).
- [22] M. Geisler, X. Cui, J. Wang, T. Rindzevicius, L. Gammelgaard, B. S. Jessen, P. A. D. Gonçalves, F. Todisco, P. Bøggild, A. Boisen, M. Wubs, N. A. Mortensen, S. Xiao, and N. Stenger, Single-Crystalline Gold Nanodisks on WS<sub>2</sub> Mono- and Multilayers for Strong Coupling at Room Temperature, *ACS Photonics* **6**, 994 (2019).
- [23] B. Munkhbat, D. G. Baranov, A. Bisht, M. A. Hoque, B. Karpiak, S. P. Dash, and T. Shegai, Electrical Control of Hybrid Monolayer Tungsten Disulfide–Plasmonic Nanoantenna Light–Matter States at Cryogenic and Room Temperatures, *ACS Nano* **14**, 1196 (2020).
- [24] O. Painter, R. K. Lee, A. Scherer, A. Yariv, J. D. O’Brien, P. D. Dapkus, and I. Kim, Two-dimensional photonic band-gap defect mode laser, *Science* **284**, 1819 (1999).
- [25] Y. Akahane, T. Asano, B. S. Song, and S. Noda, High-Q photonic nanocavity in a two-dimensional photonic crystal, *Nature* **425**, 944 (2003).
- [26] Y. Ota, R. Katsumi, K. Watanabe, S. Iwamoto, and Y. Arakawa, Topological photonic crystal nanocavity laser, *Commun. Phys.* **1**, 4 (2018).
- [27] C. Ruppert, B. Aslan, and T. F. Heinz, Optical Properties and Band Gap of Single- and Few-Layer MoTe<sub>2</sub> Crystals, *Nano Lett.* **14**, 6231 (2014).
- [28] H. Fang, J. Liu, Q. Lin, R. Su, Y. Wei, T. F. Krauss, J. Li, Y. Wang, and X. Wang, Laser-Like Emission from a Sandwiched MoTe<sub>2</sub> Heterostructure on a Silicon Single-Mode Resonator, *Adv. Opt. Mater.* **7**, 5 (2019).
- [29] D. Rosser, D. Gerace, Y. Chen, Y. Liu, J. Whitehead, A. Ryou, L. C. Andreani, and A. Majumdar, Dispersive coupling between MoSe<sub>2</sub> and an integrated zero-dimensional nanocavity, *Opt. Mater. Express* **12**, 59 (2022).
- [30] C. Qian, V. Villafañe, P. Soubelet, A. Hötger, T. Taniguchi, K. Watanabe, N. P. Wilson, A. V. Stier, A. W. Holleitner, and J. J. Finley, Nonlocal Exciton-Photon Interactions in Hybrid High- Q Beam Nanocavities with Encapsulated MoS<sub>2</sub> Monolayers, *Phys. Rev. Lett.* **128**, 237403 (2022).
- [31] J. T. Robinson, C. Manolatou, L. Chen, and M. Lipson, Ultrasmall mode volumes in dielectric optical microcavities, *Phys. Rev. Lett.* **95**, 1 (2005).
- [32] S. Hu and S. M. Weiss, Design of Photonic Crystal Cavities for Extreme Light Concentration, *ACS Photonics* **3**, 1647 (2016).
- [33] H. Choi, M. Heuck, and D. Englund, Self-Similar Nanocavity Design with Ultrasmall Mode Volume for Single-Photon Nonlinearities, *Phys. Rev. Lett.* **118**, 1 (2017).
- [34] S. Hu, M. Khater, R. Salas-Montiel, E. Kratschmer, S. Engelmann, W. M. Green, and S. M. Weiss, Experimental realization of deep-subwavelength confinement in dielectric optical resonators, *Sci. Adv.* **4**, (2018).
- [35] A. N. Babar, T. A. S. Weis, K. Tsoukalas, S. Kadkhodazadeh, G. Arregui, B. Vosoughi Lahijani, and S. Stobbe, Self-assembled photonic cavities with atomic-scale confinement, *Nature* **624**, 57 (2023).
- [36] M. Albrechtsen, B. Vosoughi Lahijani, R. E. Christiansen, V. T. H. Nguyen, L. N. Casses, S. E. Hansen, N. Stenger, O. Sigmund, H. Jansen, J. Mørk, and S. Stobbe, Nanometer-scale photon confinement in topology-optimized dielectric cavities, *Nat. Commun.* **13**, 6281 (2022).
- [37] M. Xiong, R. E. Christiansen, F. Schröder, Y. Yu, L. N. Casses, E. Semenova, K. Yvind, N. Stenger, O. Sigmund, and

- J. Mørk, Experimental realization of deep sub-wavelength confinement of light in a topology-optimized InP nanocavity, *Opt. Mater. Express* **14**, 397 (2024).
- [38] J. S. Jensen and O. Sigmund, Topology optimization for nano-photonics, *Laser Photonics Rev.* **5**, 308 (2011).
- [39] S. Molesky, Z. Lin, A. Y. Piggott, W. Jin, J. Vucković, and A. W. Rodriguez, Inverse design in nanophotonics, *Nat. Photonics* **12**, 659 (2018).
- [40] F. Wang, R. E. Christiansen, Y. Yu, J. Mørk, and O. Sigmund, Maximizing the quality factor to mode volume ratio for ultra-small photonic crystal cavities, *Appl. Phys. Lett.* **113**, (2018).
- [41] F. Wang and Y. R. Shen, General properties of local plasmons in metal nanostructures, *Phys. Rev. Lett.* **97**, 1 (2006).
- [42] G. V. Naik, V. M. Shalaev, and A. Boltasseva, Alternative plasmonic materials: Beyond gold and silver, *Adv. Mater.* **25**, 3264 (2013).
- [43] J. B. Khurgin, How to deal with the loss in plasmonics and metamaterials, *Nat. Nanotechnol.* **10**, 2 (2015).
- [44] E. V. Denning, M. Wubs, N. Stenger, J. Mørk, and P. T. Kristensen, Cavity-induced exciton localization and polariton blockade in two-dimensional semiconductors coupled to an electromagnetic resonator, *Phys. Rev. Res.* **4**, L012020 (2022).
- [45] M. V. Gurrieri, E. V. Denning, K. Seegert, P. T. Kristensen, and J. Mørk, Dynamics and condensation of polaritons in an optical nanocavity coupled to two-dimensional materials, *Phys. Rev. B* **109**, 1 (2024).
- [46] M. Abutoama, G. Kountouris, J. Mørk, and P. T. Kristensen, Modal approach to the coupling strength of quantum emitters in electromagnetic resonators, *Phys. Rev. B* **110**, 195434 (2024).
- [47] G. Dong, A. N. Babar, R. E. Christiansen, S. E. Hansen, S. Stobbe, Y. Yu, and J. Mørk, Enhancement and speed-up of carrier dynamics in a dielectric nanocavity with deep sub-wavelength confinement, arXiv:2412.08471.
- [48] G. Kountouris, A. S. Darket, L. Vestergaard, E. V. Denning, J. Mørk, and P. T. Kristensen, Lithographically defined quantum dot with subwavelength confinement of light, *Phys. Rev. B* **110**, L241301 (2024).
- [49] M. Xiong, Y. Yu, Y. Berdnikov, S. K. Borregaard, A. H. Dubré, E. Semenova, K. Yvind, and J. Mørk, A nanolaser with extreme dielectric confinement, arXiv:2412.02844.
- [50] E. V. Denning, M. Wubs, N. Stenger, J. Mørk, and P. T. Kristensen, Quantum theory of two-dimensional materials coupled to electromagnetic resonators, *Phys. Rev. B* **105**, 85306 (2022).
- [51] A. Delteil, T. Fink, A. Schade, S. Höfling, C. Schneider, and A. İmamoğlu, Towards polariton blockade of confined exciton-polaritons, *Nat. Mater.* **18**, 219 (2019).
- [52] K. Momma and F. Izumi, VESTA 3 for three-dimensional visualization of crystal, volumetric and morphology data, *J. Appl. Crystallogr.* **44**, 1272 (2011).
- [53] A. Jain, S. P. Ong, G. Hautier, W. Chen, W. D. Richards, S. Dacek, S. Cholia, D. Gunter, D. Skinner, G. Ceder, and K. A. Persson, Commentary: The Materials Project: A materials genome approach to accelerating materials innovation, *APL Mater.* **1**, (2013).
- [54] G. Kountouris, J. Mørk, E. V. Denning, and P. T. Kristensen, Modal properties of dielectric bowtie cavities with deep sub-wavelength confinement, *Opt. Express* **30**, 40367 (2022).
- [55] B. Chen, H. Sahin, A. Suslu, L. Ding, M. I. Bertonni, F. M. Peeters, and S. Tongay, Environmental Changes in MoTe<sub>2</sub> Excitonic Dynamics by Defects-Activated Molecular Interaction, *ACS Nano* **9**, 5326 (2015).
- [56] O. A. Ajayi, J. V. Ardelean, G. D. Shepard, J. Wang, A. Antony, T. Taniguchi, K. Watanabe, T. F. Heinz, S. Strauf, X. Y. Zhu, and J. C. Hone, Approaching the intrinsic photoluminescence linewidth in transition metal dichalcogenide monolayers, *2D Mater.* **4**, (2017).
- [57] F. Cadiz, E. Courtade, C. Robert, G. Wang, Y. Shen, H. Cai, T. Taniguchi, K. Watanabe, H. Carrere, D. Lagarde, M. Manca, T. Amand, P. Renucci, S. Tongay, X. Marie, and B. Urbaszek, Excitonic Linewidth Approaching the Homogeneous Limit in MoS<sub>2</sub>-Based van der Waals Heterostructures, *Phys. Rev. X* **7**, 021026 (2017).
- [58] B. Han, C. Robert, E. Courtade, M. Manca, S. Shree, T. Amand, P. Renucci, T. Taniguchi, K. Watanabe, X. Marie, L. E. Golub, M. M. Glazov, and B. Urbaszek, Exciton States in Monolayer MoSe<sub>2</sub> and MoTe<sub>2</sub> Probed by Upconversion Spectroscopy, *Phys. Rev. X* **8**, 1 (2018).
- [59] F. Schröder, M. P. van Exter, M. Xiong, G. Kountouris, M. Wubs, P. T. Kristensen, and N. Stenger, Confocal polarization tomography of dielectric nanocavities, arXiv:2412.12943.
- [60] E. S. C. Ching, P. T. Leung, A. M. van den Brink, W. M. Suen, S. S. Tong, and K. Young, Quasinormal-mode expansion for waves in open systems, *Reviews of Modern Physics* **70**, 1545 (1998).
- [61] E. A. Muljarov, W. Langbein, and R. Zimmermann, Brillouin-wigner perturbation theory in open electromagnetic systems, *EPL (Europhysics Letters)* **92**, 50010 (2010).
- [62] P. T. Kristensen and S. Hughes, Modes and mode volumes of leaky optical cavities and plasmonic nanoresonators, *ACS Photonics* **1**, 2 (2013).
- [63] P. Lalanne, W. Yan, K. Vynck, C. Sauvan, and J.-P. Hugonin, Light interaction with photonic and plasmonic resonances, *Laser & Photonics Reviews* **12**, 1700113 (2018).
- [64] P. T. Kristensen, K. Herrmann, F. Intravaia, and K. Busch, Modeling electromagnetic resonators using quasinormal modes, *Adv. Opt. Photon.* **12**, 612 (2020).

- [65] S. Both and T. Weiss, Resonant states and their role in nanophotonics, *Semiconductor Science and Technology* **37**, 013002 (2021).
- [66] C. Carlson, R. Salzwedel, M. Selig, A. Knorr, and S. Hughes, Strong coupling regime and hybrid quasinormal modes from a single plasmonic resonator coupled to a transition metal dichalcogenide monolayer, *Phys. Rev. B* **104**, 125424 (2021).
- [67] D. Xiao, G. B. Liu, W. Feng, X. Xu, and W. Yao, Coupled spin and valley physics in monolayers of MoS<sub>2</sub> and other group-VI dichalcogenides, *Phys. Rev. Lett.* **108**, 1 (2012).
- [68] F. Todisco, R. Malureanu, C. Wolff, P. A. D. Gonçalves, A. S. Roberts, N. A. Mortensen, and C. Tserkezis, Magnetic and electric Mie-exciton polaritons in silicon nanodisks, *Nanophotonics* **9**, 803 (2020).
- [69] O. Bleu, K. Choo, J. Levinsen, and M. M. Parish, Dissipative light-matter coupling and anomalous dispersion in nonideal cavities, *Phys. Rev. A* **109**, 1 (2024).
- [70] S. Helmrich, R. Schneider, A. W. Achtstein, A. Arora, B. Herzog, S. M. de Vasconcellos, M. Kolarczik, O. Schöps, R. Bratschitsch, U. Woggon, and N. Owschimikow, Exciton-phonon coupling in mono- and bilayer MoTe<sub>2</sub>, *2D Mater.* **5**, 45007 (2018).
- [71] E. Dimopoulos, A. Sakanas, A. Marchevsky, M. Xiong, Y. Yu, E. Semenova, J. Mørk, and K. Yvind, Electrically-driven Photonic Crystal Lasers with Ultra-low Threshold, *Laser Photonics Rev.* **2200109**, 1 (2022).
- [72] R. V. Gorbachev, I. Riaz, R. R. Nair, R. Jalil, L. Britnell, B. D. Belle, E. W. Hill, K. S. Novoselov, K. Watanabe, T. Taniguchi, A. K. Geim, and P. Blake, Hunting for Monolayer Boron Nitride: Optical and Raman Signatures, *Small* **7**, 465 (2011).
- [73] P. Holm, *Atomically precise patterning by thermal scanning probe lithography*, Master's thesis, Technical University of Denmark (DTU) (2024).
- [74] A. Castellanos-Gomez, M. Buscema, R. Molenaar, V. Singh, L. Janssen, H. S. Van Der Zant, and G. A. Steele, Deterministic transfer of two-dimensional materials by all-dry viscoelastic stamping, *2D Mater.* **1**, 10.1088/2053-1583/1/1/011002 (2014).
- [75] P. J. Zomer, M. H. Guimarães, J. C. Brant, N. Tombros, and B. J. Van Wees, Fast pick up technique for high quality heterostructures of bilayer graphene and hexagonal boron nitride, *Appl. Phys. Lett.* **105**, 10.1063/1.4886096 (2014).
- [76] F. Pizzocchero, L. Gammelgaard, B. S. Jessen, J. M. Caridad, L. Wang, J. Hone, P. Bøggild, and T. J. Booth, The hot pick-up technique for batch assembly of van der Waals heterostructures, *Nat. Commun.* **7**, 10.1038/ncomms11894 (2016).
- [77] J. Kutrowska-Girzycka, E. Zieba-Ostójk, D. Biegańska, M. Florian, A. Steinhoff, E. Rogowicz, P. Mrowiński, K. Watanabe, T. Taniguchi, C. Gies, S. Tongay, C. Schneider, and M. Syperek, Exploring the effect of dielectric screening on neutral and charged-exciton properties in monolayer and bilayer MoTe<sub>2</sub>, *Appl. Phys. Rev.* **9**, 10.1063/5.0089192 (2022).
- [78] P. T. Kristensen, R.-C. Ge, and S. Hughes, Normalization of quasinormal modes in leaky optical cavities and plasmonic resonators, *Phys. Rev. A* **92**, 053810 (2015).
- [79] L. Meckbach, J. Hader, U. Huttner, J. Neuhaus, J. T. Steiner, T. Stroucken, J. V. Moloney, and S. W. Koch, Ultrafast band-gap renormalization and build-up of optical gain in monolayer MoTe<sub>2</sub>, *Phys. Rev. B* **101**, 1 (2020).
- [80] S. Edalati-Boostan, C. Cocchi, and C. Draxl, MoTe<sub>2</sub> as a natural hyperbolic material across the visible and the ultraviolet region, *Phys. Rev. Mater.* **4**, 1 (2020).
- [81] S. Haastrup, M. Strange, M. Pandey, T. Deilmann, P. S. Schmidt, N. F. Hinsche, M. N. Gjerding, D. Torelli, P. M. Larsen, A. C. Riis-Jensen, J. Gath, K. W. Jacobsen, J. Jørgen Mortensen, T. Olsen, and K. S. Thygesen, The Computational 2D Materials Database: high-throughput modeling and discovery of atomically thin crystals, *2D Mater.* **5**, 042002 (2018).
- [82] D. V. Grudinin, G. A. Ermolaev, D. G. Baranov, A. N. Toksumakov, K. V. Voronin, A. S. Slavich, A. A. Vyshnevyy, A. B. Mazitov, I. A. Kruglov, D. A. Ghazaryan, A. V. Arsenin, K. S. Novoselov, and V. S. Volkov, Hexagonal boron nitride nanophotonics: a record-breaking material for the ultraviolet and visible spectral ranges, *Mater. Horizons* **10**, 2427 (2023).
- [83] G. D. Pettit and W. J. Turner, Refractive Index of InP, *J. Appl. Phys.* **36**, 2081 (1965).
- [84] J. A. McCaulley, V. M. Donnelly, M. Vernon, and I. Taha, Temperature dependence of the near-infrared refractive index of silicon, gallium arsenide, and indium phosphide, *Phys. Rev. B* **49**, 7408 (1994).
- [85] D. R. Danielsen, N. Lassaline, S. J. Linde, M. V. Nielsen, X. Zambrana-Puyalto, A. Sarbajna, D. H. Nguyen, T. J. Booth, N. Stenger, and S. Raza, Fourier-Tailored Light-Matter Coupling in van der Waals Heterostructures (2025), arXiv:2502.02114.
- [86] F. Hu and Z. Fei, Recent Progress on Exciton Polaritons in Layered Transition-Metal Dichalcogenides, *Adv. Opt. Mater.* **8**, 1 (2020)